# 1
# Introduction to Thin-Film Photovoltaics

*Thomas Kirchartz, Daniel Abou-Ras, and Uwe Rau*

## 1.1
## Introduction

From the early days of photovoltaics until today, thin-film solar cells have always competed with technologies based on single-crystal materials such as Si and GaAs. Owing to their amorphous or polycrystalline nature, thin-film solar cells always suffered from power-conversion efficiencies lower than those of the bulk technologies. This drawback was and still is counterbalanced by several inherent advantages of thin-film technologies. Because in the early years of photovoltaics space applications were the driving force for the development of solar cells, the argument in favor of thin films was their potential lighter weight as compared with bulk materials.

An extended interest in solar cells as a source of renewable energy emerged in the mid-1970s as the limitations of fossil energy resources were widely recognized. For terrestrial power applications the cost arguments and the superior energy balance strongly favored thin films. However, from the various materials under consideration in the 1950s and 1960s, only four thin-film technologies, namely, hydrogenated amorphous Si (a-Si:H) and the polycrystalline heterojunction systems CdS/$Cu_xS$, CdS/CdTe, and CdS/Cu(In,Ga)$Se_2$, entered pilot production. Activities in the CdS/$Cu_xS$ system stopped at the beginning of the 1980s because of stability problems. At that time amorphous silicon became the front runner in thin-film technologies keeping almost constantly a share of about 10% in a constantly growing photovoltaic market with the remaining 90% kept by crystalline Si. Despite their high efficiency potential, polycrystalline heterojunction solar cells based on CdTe and Cu(In,Ga)$Se_2$ did not play an economic role until the turn of the century.

During the accelerated growth of the worldwide photovoltaic market since the year 2000, the market share of thin-film technologies was again at a level at or above 10%, with an increasing contribution of CdTe and Cu(In,Ga)$Se_2$. With annual production figures in the GW range, thin-film photovoltaics has become a multibillion-dollar business. In order to expand this position, further dramatic cost reduction is required combined with a substantial increase of

*Advanced Characterization Techniques for Thin Film Solar Cells*, Second Edition.
Edited by Daniel Abou-Ras, Thomas Kirchartz, and Uwe Rau.
© 2016 Wiley-VCH Verlag GmbH & Co. KGaA. Published 2016 by Wiley-VCH Verlag GmbH & Co. KGaA.

module efficiency. In this context, material and device characterization becomes an important task not only for quality control in an expanding industry but remains also at the very heart of further technological progress.

In addition to the three inorganic thin-film technologies, also solar cells containing one or more organic materials were studied in particular from the 1990s onward. Two main variants of such organic solar cells are developed. The first one, the dye-sensitized solar cell (DSSC), uses organic dyes (later also inorganic nanoparticles) as light absorbers. In order to be able to use any well-absorbing material without putting any constraint on its ability to transport electrons and holes, a monolayer of that well-absorbing material (the dye) was attached to a mesoporous scaffold (usually made up of $TiO_2$) which was then immersed in a liquid and later also solid-state electrolyte infiltrating the pores of the scaffold. The tasks of light absorption as well as transport of the negative and positive charge carrier would then be performed by different materials, namely, the dye, the scaffold, and the electrolyte in this order. The second variant of an organic solar cell distributed the three tasks mentioned above over two materials: The first, usually a polymer, was used for light absorption and hole transport, while the second material (usually a fullerene) was used for electron transport and to a lesser degree also for light absorption. These technologies surpassed efficiencies of 10% and saw some attempts at commercialization, though so far on a smaller scale than, for example, CdTe. Within the last few years, the seemingly clear boundaries between the fields of organic and inorganic solar cells have started to become blurred by the advent of hybrid (organic–inorganic) metal-halide perovskites. The most widely used material in this class is $CH_3NH_3PbI_3$, which has an organic molecule ($CH_3NH_3$) on the A lattice position, lead on the B position, and iodine on the X position (for an $ABX_3$ perovskite). $CH_3NH_3PbI_3$ is one example of a class of materials that managed to surpass 20% efficiency on a cell level – the first time for an "organic" semiconductor. Given that these highly efficient perovskite solar cells are able to combine the tasks of light absorption as well as electron and hole transport just like the three typical inorganic thin-film technologies, the demands for and the methods used for device and material characterization in these perovskites are in many respects quite similar to the ones needed for inorganic thin-film solar cells.

The present book comprises a large range of characterization techniques used for photovoltaic devices and materials. The examples shown in the chapters concentrate on the three inorganic thin-film technologies – thin-film Si (a-Si:H, microcrystalline μc-Si:H, and combinations of both forming a tandem solar cell) – and the two heterojunction systems CdS/CdTe as well as $CdS/Cu(In,Ga)(Se,S)_2$ but sometimes include examples from organic and perovskite devices as well. These thin-film technologies have in common that they consist of layer sequences made up from disordered semiconductor materials that are deposited onto a supporting substrate or superstrate. This layer structure and the use of disordered materials define a fundamental difference to devices based on crystalline c-Si where a self-supporting Si wafer is transformed into a solar cell via a solid-state diffusion of dopant atoms. Thus, there are only the front

and the back surface as critical interfaces in the classical wafer solar cell (with the notable exception of the a-Si:H/c-Si heterojunction solar cell). In thin-film solar cells, the number of functional layers can amount to up to eight and more. Some of these layers have thicknesses as low as 10 nm. In large-area modules, these layers homogeneously cover areas of up to 6 $m^2$. These special features of the thin-film photovoltaic technologies define the field for the characterization techniques discussed in the present book.

Electrical characterization, electroluminescence and photoluminescence, capacitance spectroscopy, and characterization of light trapping as considered in Chapters 2–4 as well as 6, 8, 10, and 11 are common analysis techniques for photovoltaic devices. However, the specific properties of the thin-film systems like the disordered nature of the materials, the importance of features at the nanometer scale, and the fact that the film thicknesses are of the order or below the wavelength of visible light account for the special aspects to be considered when using these techniques. Chapters 5, 7, 8, and 9 deal with techniques like ellipsometry, photothermal deflection spectroscopy, the steady-state photocarrier grating method, and time-of-flight analysis, which are thin-film-specific methods, and moreover, some were even invented within the field of thin-film photovoltaics. Chapters 12–20 discuss classical methods for material characterization, each of them having special importance for at least one photovoltaic technology. Again, the specific features of photovoltaic thin films like the importance of dangling bonds and hydrogen passivation in disordered Si, the need for physical and chemical material analysis at the nanometer scale, or the prominence of interface chemistry and physics in thin-film solar cells define the focus of these chapters. Chapters 21–24 at the end of the handbook deal with the theoretical description of materials and devices. *Ab initio* modeling of semiconductor materials is indispensable, because even the basic physical properties of some of the wide variety of compounds and alloys used in thin-film photovoltaics are not satisfactorily known. Finally, successful modeling of the finished devices may be looked at as the definitive proof of our understanding of materials and interfaces.

The present introductory chapter yields a brief general introduction into the basic principles of photovoltaics, highlighting the specific material and device properties that are relevant for thin-film solar cells.

## 1.2 The Photovoltaic Principle

The temperature difference between the surface of the sun with a temperature of $T = 5800$ K and the surface of the earth ($T = 300$ K) is the driving force of any solar-energy conversion technology. Solar cells and solar modules directly convert the solar radiation into electricity using the internal photoelectric effect. Thus, any solar cell needs a photovoltaic absorber material that is not only able to absorb the incoming light efficiently but also to create mobile charge carriers, electrons and

holes, that are separated at the terminals of the device without significant loss of energy. Note that in *organic* absorber materials most light-absorption processes generate excitons and a first step of charge separation is necessary in order to dissociate the exciton into free carriers. In contrast, the low binding energy of excitons in *inorganic* semiconductors makes absorption and generation of mobile charge carriers in appropriate absorber materials of this type virtually identical. Thus, after light absorption electrons and holes are present in the absorber and must be directed toward the two different contacts of the absorber, that is, the final charge carrier separation step.

For a semiconductor acting as a photovoltaic absorber, its band-gap energy $E_g$ is the primary quantity defining how many charge carriers are generated from solar photons with energy $E \geq E_g$. Maximizing the number of photons contributing to the short-circuit current density of a solar cell would require minimizing $E_g$. Since photogenerated electron–hole pairs thermalize to the conduction-band and valence-band edges after light absorption, the generated energy per absorbed photon corresponds to $E_g$ regardless of the initial photon energy $E$. Thus, maximizing the band-gap energy $E_g$ maximizes the available energy per absorbed photon. Therefore, one intuitively expects that an optimum band-gap energy exists between $E_g = 0$, maximizing the generated electron–hole pairs, and $E_g \to \infty$, maximizing the generated energy contained in a single electron–hole pair. Quantitatively, this consideration is reflected in the dependence of the maximum achievable conversion efficiency of a single-band-gap photovoltaic absorber material as discussed in the following section.

### 1.2.1
### The Shockley–Queisser Theory

The maximum power-conversion efficiency of a solar cell consisting of single semiconducting absorber material with band-gap energy $E_g$ is described by the Shockley–Queisser (SQ) [1] limit. In its simplest form, the SQ limit relies on four basic assumptions: (i) The probability for the absorption of solar light by the generation of a single electron–hole pair in the photovoltaic absorber material is unity for all photon energies $E \geq E_g$ and zero for $E < E_g$. (ii) All photogenerated charge carriers thermalize to the band edges. (iii) The collection probability for all photogenerated electron–hole pairs at short circuit is unity. (iv) The only loss mechanism in excess of the nonabsorbed photons of (i) and the thermalization losses in (ii) are spontaneous emission of photons by radiative recombination of electron–hole pairs as required by the principle of detailed balance.

In order to calculate the maximum available short-circuit current $J_{sc,SQ}$ as defined by (iii), we need the incoming photon flux $\phi_{inc}$ and the absorptance $A(E)$ defining the percentage of the incoming light at a certain photon energy $E$ that is absorbed and not reflected or transmitted. The simplest approximation defined for an ideal absorber by condition (i) is a step function, that is, $A(E) = 1$ (for $E > E_g$) and $A(E) = 0$ (for $E < E_g$). Then we have under short-circuit conditions

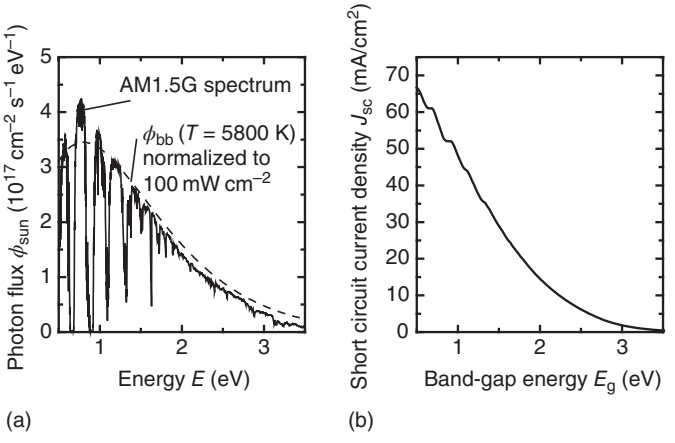


**Figure 1.1** (a) Comparison of the AM1.5G spectrum with the blackbody spectrum of a body with a temperature $T = 5800$ K. Both spectra are normalized such that the power density is 100 mW/cm$^2$. (b) Using the AM1.5G spectrum and Equation (1.1), we obtain the short-circuit current density $J_{sc,SQ}$ in the Shockley–Queisser limit as a function of the band-gap energy $E_g$ of the solar absorber.

(i.e., applied voltage $V = 0$ V)

$$J_{sc,SQ} = q\int_0^\infty A(E)\phi_{inc}(E)\mathrm{d}E = q\int_{E_g}^\infty \phi_{inc}(E)\mathrm{d}E, \tag{1.1}$$

where $q$ denotes the elementary charge.

Figure 1.1a compares the spectral photon flux corresponding to the terrestrial AM1.5G norm spectrum with the blackbody spectrum at $T = 5800$ K, both spectra normalized to a power density of 100 mW/cm$^2$. Figure 1.1b illustrates the maximum short-circuit current density that is possible for a given band-gap energy $E_g$ according to Equation 1.2.

Since light absorption by generation of free carriers and light emission by recombination of electron–hole pairs are interconnected by the principle of detailed balance, in thermodynamic equilibrium the photon emission $\phi_{em}$ is connected to the absorptance via Kirchhoff's law $\phi_{em} = A(E)\phi_{bb}(E, T)$, where $\phi_{bb}(E, T)$ is the blackbody spectrum at temperature $T$.

In an ideal solar cell under applied voltage bias, we use Würfel's [2] generalization of Kirchhoff's law to describe the recombination current $J_{rec,SQ}$ for radiative recombination according to

$$J_{rec,SQ} = q\int_0^\infty A(E)\phi_{bb}(E,T)\exp\left(\frac{qV}{kT}\right)\mathrm{d}E = q\int_{E_g}^\infty \phi_{bb}(E,T)\exp\left(\frac{qV}{kT}\right)\mathrm{d}E, \tag{1.2}$$

where the second equality again results from the assumption of a sharp band-gap energy $E_g$. Thus, Equation 1.2 describes the current density of a solar cell in

the dark if only radiative recombination of carriers is considered corresponding to condition (iv) and the carriers have the temperature $T$ of the solar cell according to condition (ii). The total current density $J$ under illumination is a superposition of this radiative recombination current density and the short-circuit current density defined in Equation 1.1. Thus, we can write

$$J(V) = J_{\mathrm{rec,SQ}}(V) - J_{\mathrm{sc,SQ}} = q\int_{E_g}^{\infty} \phi_{\mathrm{bb}}(E)\mathrm{d}E \exp\left(\frac{qV}{kT}\right) - q\int_{E_g}^{\infty} \phi_{\mathrm{inc}}(E)\mathrm{d}E. \quad (1.3)$$

There are two contributions to the incoming photon flux $\phi_{\mathrm{inc}}$, that is, the spectrum $\phi_{\mathrm{sun}}$ of the sun and the photon flux $\phi_{\mathrm{bb}}$ from the environment which has the same temperature as the sample. When we replace the incoming photon flux $\phi_{\mathrm{inc}}$ with the sum $\phi_{\mathrm{sun}} + \phi_{\mathrm{bb}}$, Equation 1.3 simplifies to

$$J(V) = q\int_{E_g}^{\infty} \phi_{\mathrm{bb}}(E)\mathrm{d}E \left[\exp\left(\frac{qV}{kT}\right) - 1\right] - q\int_{E_g}^{\infty} \phi_{\mathrm{sun}}(E)\mathrm{d}E, \quad (1.4)$$

which is a typical diode equation with an additional photocurrent only due to the extra illumination from the sun. Now it is obvious that for 0 excess illumination and 0 V applied, the current becomes 0.

Figure 1.2 shows the current density/voltage ($J/V$) curves of an ideal solar cell according to Equation 1.4 for three different band-gap energies $E_g = 0.8$, 1.4, and

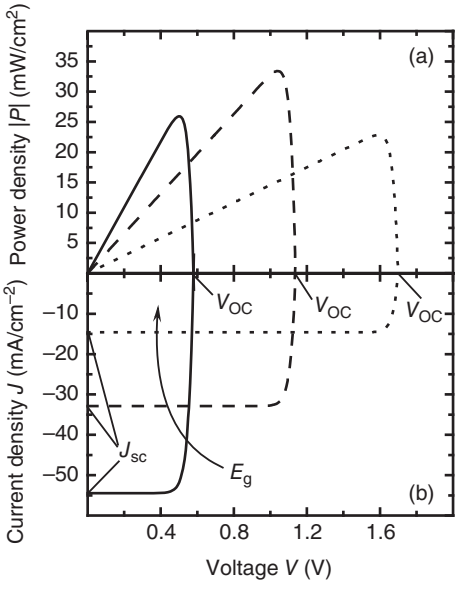


**Figure 1.2** (a) Power density/voltage curves and (b) current density/voltage ($J/V$) curves of three ideal solar cells with band gaps $E_g = 0.8$, 1.4, and 2.0 eV, respectively. The higher the band gap $E_g$, the higher the open-circuit voltage $V_{oc}$, that is, the intercept of both power density and current density with the voltage axis. However, a higher band gap also leads to a decreased short-circuit current $J_{sc}$ (cf. Figure 1.1b). The curves are calculated using Equation 1.4.

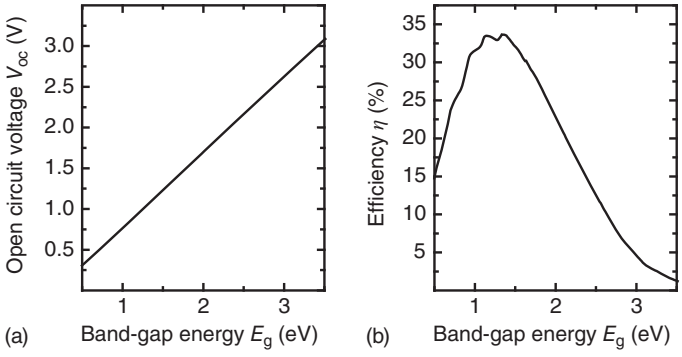


**Figure 1.3** (a) Open-circuit voltage and (b) conversion efficiency as a function of the band-gap energy $E_g$ in the Shockley–Queisser limit using an AM1.5G spectrum as illumination. The optimum band-gap energies for single-junction solar cells are in the range of 1.1 eV $< E_g <$ 1.4 eV with maximum conversion efficiencies around $\eta = 33\%$ under unconcentrated sunlight.

2.0 eV. If we evaluate Equation 1.4 under open-circuit conditions, that is, at $J = 0$, we find the maximum possible voltage in the fourth quadrant of the coordinate system in Figure 1.2. This voltage is called the open-circuit voltage $V_{oc}$ and follows from Equation 1.4 as

$$V_{oc} = \frac{kT}{q} \ln\left( \frac{\int_{E_g}^{\infty} \phi_{sun}(E)\mathrm{d}E}{\int_{E_g}^{\infty} \phi_{bb}(E)\mathrm{d}E} + 1 \right) = \frac{kT}{q} \ln\left( \frac{J_{sc,SQ}}{J_{0,SQ}} + 1 \right). \tag{1.5}$$

Here, $J_{0,SQ}$ is the saturation current density in the SQ limit, that is, the smallest possible saturation current density for a semiconductor of a given band gap. The open-circuit voltage increases nearly linearly with increasing band gap as shown in Figure 1.3a.

From Equation 1.4, the power density follows by multiplication with the voltage. The efficiency $\eta$ is then the maximum of the negative power density,[1)] that is,

$$\eta = \frac{-\max(J(V)V)}{P_{opt}} = \frac{-\max(J(V)V)}{\int_{E_g}^{\infty} E\phi_{sun}(E)\mathrm{d}E}. \tag{1.6}$$

Figure 1.3b shows the final result of the SQ theory: the efficiency as a function of the band-gap energy for illumination with the AM1.5G spectrum depicted in Figure 1.1a.

1) Negative current density means here that the current density is opposite to the current density any passive element would have. A negative power density means then that energy is extracted from the device and not dissipated in the device as it would happen in a diode, which is not illuminated.

### 1.2.2 From the Ideal Solar Cell to Real Solar Cells

The universality and simplicity of the SQ limit are due to the fact that all internal details of the solar cell are irrelevant for its derivation. However, these hidden details are the practical subjects of research on real solar cells and especially on thin-film solar cells. It is important to understand that some of these details idealized (or neglected) by the original SQ theory are not in conflict with the detailed balance principle [3].

Firstly, starting from a step function like absorptance toward a more complex spectral dependence of $A(E)$ is not in conflict with the radiative recombination limit (cf. Equations 2.1 and 2.2). A continuous transition from zero to unity is expected for any semiconductor material with finite thickness. Especially for thin-film absorbers, maximizing light absorption is an important task requiring additional means to confine the light as discussed in Section 1.2.3. Moreover, the disorder in thin-film absorbers may lead to additional electronic states close to the band gap (so-called band tails or band-gap fluctuations) with a considerable contribution to light absorption and emission. In consequence, the achievable conversion efficiency is reduced even in the radiative limit [4].

Secondly, proper extraction of the photogenerated electrons and holes requires sufficiently high carrier mobilities and selectivity of the contacts to make sure that all electrons and holes are collected in the n-type and in the p-type contact. Again, these requirements are valid even when restricting the situation to radiative recombination [5]. Since mobilities in disordered thin-film materials are generally lower than in monocrystalline absorbers, charge carrier extraction is an issue to be discussed with special care (Section 1.2.4).

Finally, recombination in thin-film solar cells is dominated by nonradiative processes. Thus, especially the achieved open-circuit voltages are far below the radiative limit. Section 1.2.5 and the major part of Chapter 2 will deal with understanding the efficiency limits resulting from all sorts of nonradiative recombination. It is important to note that even when considering nonradiative recombination, we must not necessarily abandon a detailed balance approach [6, 7] (cf. Chapter 3).

### 1.2.3 Light Absorption and Light Trapping

The first requirement for any solar cell is to absorb light as efficiently as possible. Solar-cell absorbers should therefore be nontransparent for photons with energy $E > E_g$. For any solar cell but especially for thin-film solar cells, this requirement is in conflict with the goal of using as little absorber material as possible. Additionally, thinner absorbers facilitate charge extraction for materials with low mobilities and/or lifetimes of the photogenerated carriers. This is why light trapping in photovoltaic devices is of major importance. Light trapping exploits randomization of light at textured surfaces or interfaces in combination with the fact that

semiconductor absorber layers have typical refractive indices $n$ that are higher than that of air ($n = 1$) or glass ($n \approx 1.5$). Typical values for the real part of the refractive index are $n > 3.5$ in inorganic solar absorbers and $n \approx 2$ in organic materials. However, the light first has to enter the solar cell. In order to minimize reflection of incoming light at the front surface, a high refractive index is a disadvantage. The reflectance

$$R = \left(\frac{n-1}{n+1}\right)^2 \tag{1.7}$$

at the interface between air and the semiconductor (for normal incidence) will become higher, when the refractive index gets higher. However, the high reflection at the front surface is reduced by using several layers between air and absorber layer. The refractive indices of these layers increase gradually, and any large refractive index contrast (leading to strong reflection) is avoided.

For light trapping, however, a high refractive index has an advantage. When the direction of the incoming light is randomized by a scattering interface somewhere in the layer stack of the thin-film solar cell, part of the light will be guided in the solar-cell absorber by total internal reflection. The percentage of light kept in the solar cell by total internal reflection increases with the refractive index, since the critical angle $\theta_c = \arcsin(1/n)$ becomes smaller. For light with a Lambertian distribution of angles, the reflectance of the front surface for light from the inside is

$$R_i = 1 - \frac{(1-R_f)\displaystyle\int_0^{\theta_c} \cos\theta \sin\theta \mathrm{d}\theta}{\displaystyle\int_0^{\pi/2} \cos\theta \sin\theta \mathrm{d}\theta} = 1 - \frac{(1-R_f)}{n^2}. \tag{1.8}$$

Here, $R_f$ is the reflectance at the front side of the absorber for normal incidence.

To visualize the effect the absorption coefficient and light trapping has on the absorptance of a solar cell, we present some calculations for a model system. Let us assume a direct semiconductor, which have absorption coefficients of the typical form

$$\alpha = \alpha_0 \sqrt{\frac{E - E_g}{1\,\mathrm{eV}}}. \tag{1.9}$$

Then, the absorptance $A(E)$, that is, the percentage of photons that are absorbed and not reflected or transmitted at a certain photon energy, is calculated for flat surfaces and for an absorber thickness much larger than the wavelength of light with

$$A = (1-R_f)\frac{(1-\mathrm{e}^{-\alpha d})(1+R_b\mathrm{e}^{-\alpha d})}{1-R_f R_b \mathrm{e}^{-2\alpha d}}. \tag{1.10}$$

Here, $R_b$ is the reflectance at the backside. Equation 1.10 assumes an infinite number of reflections at the front and the back of the absorber layer. To calculate the real absorptance of any thin-film solar cell, it is rather useless for two reasons: (i) Thin-film solar cells usually consist of several layers and not only one, and (ii) the

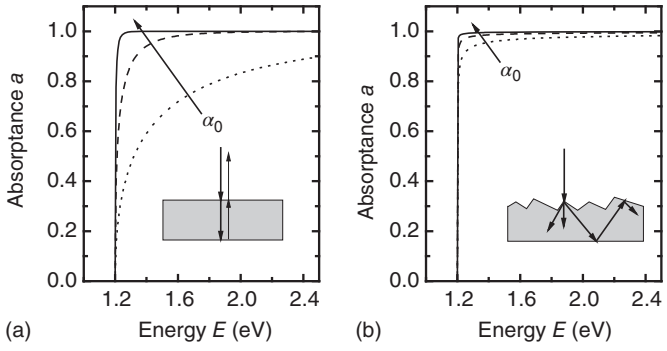


**Figure 1.4** Absorptance as a function of photon energy for (a) a flat solar cell and (b) a textured solar cell with perfect light trapping. In both cases the absorption coefficient $\alpha_0$ from Equation 1.9 is varied. The values are for both subfigures $\alpha_0 = 10^4$, $\sqrt{10} \times 10^4$, $10^5\,\mathrm{cm}^{-1}$. For the same absorption coefficient, the textured solar cell has absorptances that are much closer to the perfect step function than the flat solar cell.

layer thicknesses are of the same order than the wavelength of light and interferences cannot be neglected any more. Nevertheless Equation 1.10 is useful to test the influence of the absorption coefficient on the absorptance. Figure 1.4a compares the absorptance calculated according to Equation 1.10 for three different values of $\alpha_0$, namely, $\alpha_0 = 10^4$, $\sqrt{10} \times 10^4$, $10^5\,\mathrm{cm}^{-1}$, and for a constant thickness $d$ of the absorber of $d = 1\,\mu\mathrm{m}$. The reflectance at the front side is assumed to be $R_\mathrm{f} = 0$ and the reflectance at the backside is $R_\mathrm{b} = 1$.

To calculate the absorptance of a textured cell with light trapping, it is necessary to integrate over all angles. The resulting equations are rather complicated [8, 9]; however, a simple and useful approximation exists for the case $R_\mathrm{b} = 1$, namely, [10]

$$A = \frac{1 - R_\mathrm{f}}{1 + \dfrac{(1 - R_\mathrm{f})}{4n^2 \alpha d}}. \tag{1.11}$$

Figure 1.4b shows the result of applying the absorption coefficient defined in Equations 1.9–1.11. Again, the absorptance for the case of perfect light trapping is calculated for $\alpha_0 = 10^4$, $\sqrt{10} \times 10^4$, $10^5\,\mathrm{cm}^{-1}$, $d = 1\,\mu\mathrm{m}$, and $R_\mathrm{f} = 0$. The refractive index is assumed to be $n = 3.5$. It is obvious that for a given value of $\alpha_0$, the absorptance of the textured solar cell comes much closer to the perfect step function like absorptance of the SQ limit.

To visualize the effect of light trapping on the short-circuit current density $J_\mathrm{sc}$, Figure 1.5 compares the $J_\mathrm{sc}$ as a function of the product $\alpha_0 d$ for a flat and a Lambertian surface, that is, for absorptances calculated with Equation 1.10 and with Equation 1.11. The band gap is chosen to be $E_\mathrm{g} = 1.2\,\mathrm{eV}$ as in Figure 1.4 so the maximum $J_\mathrm{sc}$ for high $\alpha_0 d$ is the same as in the SQ limit (cf. Figure 1.1b), namely, $J_\mathrm{sc,max} \approx 40\,\mathrm{mA/cm}^2$. However, for lower $\alpha_0 d$, the $J_\mathrm{sc}$ with and without light trapping differ considerably and show the benefit from structuring the surface to enhance the scattering in the absorber layer. In reality the benefit from

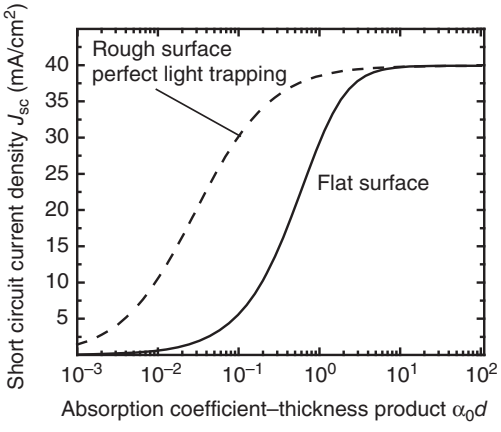


**Figure 1.5** Comparison of the short-circuit current density of a flat (solid line) and a textured solar cell (dashed line) as a function of the product of $\alpha_0$ and the thickness $d$ assuming an absorption coefficient according to Equation 1.9 (with $E_g = 1.2$ eV). Especially for low absorption coefficients relative to the device thickness (low $\alpha_0 d$), light trapping increases the short-circuit current density drastically. The refractive index used for these simulations is $n = 3.5$ independent of photon energy.

light trapping will be smaller since the light has to be reflected several times at the front and especially at the back surface, where we assumed the reflection to be perfect. In reality any back reflector will absorb part of the light parasitically, that is, the light is absorbed but no electron–hole pairs are created, which could contribute to the photocurrent.

### 1.2.4 Charge Extraction

After an electron–hole pair is generated, the charge carriers must be extracted from the absorber layer. To get a net photocurrent, the electron must leave the device at the opposite contact than the hole. This requires a built-in asymmetry that makes electrons leave the device preferentially at the electron-extracting contact (cathode) and holes at the hole-extracting contact (anode).

Figure 1.6 introduces three device geometries that induce a built-in asymmetry that helps to extract oppositely charged carriers at opposite contacts. Figure 1.6a shows the band diagram of a p–n-junction solar cell under illumination, and Figure 1.6d shows the same cell with an applied voltage $V = 0.5$ V. The simulations were done by solving the Poisson equation and the continuity equations with the software ASA, which is described in Chapter 23. As typical for most solar cells with a p–n junction, the space charge region, where the bands are steep and the electric field is high, is at the very edge of the device. Most of the device consists in our example of a p-type base layer, where the field is practically zero. The transport of minority carriers (here electrons) to the space charge region is purely

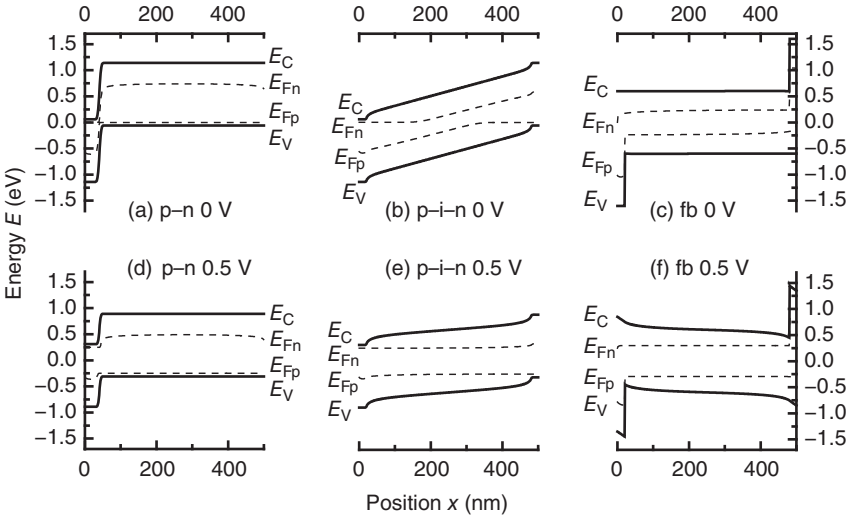


**Figure 1.6** Simulation of the band diagrams of a (a, d) p–n-junction, a (b, e) p–i–n-junction, and a (c, f) flatband (fb) solar cell under illumination. Every type of geometry is depicted under short-circuit conditions and under an applied forward bias $V = 0.5$ V.

diffusive and independent from the applied voltage. That means application of a voltage only changes the electrical potential in the space charge region but not in the much larger neutral base.

The band bending at the junction leads to an asymmetry that separates the charges. Electrons are able to diffuse to the junction and then further to the n-type region and the electron contact. In addition the p–n junction serves as a barrier for holes which are in turn extracted by the back contact. Note that in the band diagram in Figure 1.6a and d, this back contact is not selective as is the p–n junction. Therefore, also electrons can leave the device at this contact, a fact that is usually considered as contact or surface recombination (cf. Chapter 2) and might be a major loss mechanism. Cu(In,Ga)$Se_2$ solar cells are examples for p–n (hetero)junctions.

For some disordered semiconductors like amorphous silicon, the electronic quality of doped layers is very poor. In addition, the mobilities and diffusion lengths are small; thus purely diffusive transport would not lead to efficient charge extraction. The solution to this problem is the so-called p–i–n-junction diode. Here the doped layers are very thin compared to the complete thickness of the diode. The largest share of the complete absorber thickness is occupied by an intrinsic, that is, undoped layer, in between the n- and p-type regions. Figure 1.6a shows the band diagram of such a p–i–n-junction solar cell under illumination, and Figure 1.6d shows the same cell with an applied voltage $V = 0.5$ V. At short circuit, the region with a nonzero electric field extends over the complete intrinsic layer. Only directly at the contacts the field is relatively small. When a forward

voltage is applied to the cell, the electric field becomes smaller as shown in Figure 1.6d. Solar cells made from a-Si:H as well as a-Si:H/μc-SiH tandem cells use the p–i–n configuration.

Both p–n-junction and p–i–n-junction solar cells have a built-in field, meaning that the bands are bended due to the different conductivity type of the layers. Theoretically, such a band bending is not necessary to separate charges as can be shown by a gedanken experiment [11]. Figure 1.6c shows the band diagram of a hypothetical flatband solar cell under short-circuit conditions. Like the p–i–n-junction solar cell, the flatband solar cell has an intrinsic layer sandwiched between two other layers that induce the asymmetry for charge separation. In this case, the asymmetry is not due to band bending and differently doped layers but instead due to band offsets at the heterojunction between two materials with different band gaps. Let us assume we find one contact material with zero band offset for the electrons and a high (in this case 1 eV) band offset for the holes and another material with the exact inverse properties. In this case the band diagram is completely flat at short circuit apart from the two band offsets. Like in the p–n-junction solar cell, the charge separation at short circuit is arranged via diffusive transport that is effective, when the diffusion length is high enough.

Under applied voltage the drawback of the flatband solar cell becomes obvious. The voltage has to drop somewhere over the absorber layer leading to an electric field, which creates a barrier for the extraction of charge carriers. While for a p–i–n-junction solar cell the field-assisted charge extraction becomes weaker with applied voltage, in a flatband solar cell the field hinders charge separation. This is why we consider in the following the flatband solar cell as a paradigmatic example for a device that exhibits poor charge separation properties. In fact, some typical features that show up in the numerical simulations in the following are indicative in practical (but faulty) devices for problems due to nonideal contact properties.

To illustrate the basic properties of the solar-cell structures introduced in Figure 1.6, we simulated the current/voltage curves for two different mobilities $\mu$ of electrons and holes. The recombination in the device was assumed to be dominated by one defect in the middle of the device with a Shockley–Read–Hall lifetime (see Section 1.2.5) $\tau = 100\,\text{ns}$ for electrons and holes. In addition, we assumed a surface recombination velocity $S = 10^5\,\text{cm/s}$ for the holes at the electron contact ($x = 0$) and the electrons at the hole contact ($x = 500\,\text{nm}$). The results are presented in Figure 1.7a ($\mu = 10^{-1}\,\text{cm}^2/\text{V s}$) and Figure 1.7b ($\mu = 10^{1}\,\text{cm}^2/\text{V s}$), demonstrating that short-circuit current density is substantially decreased when turning from the high to the low mobility. The fill factor FF, that is,

$$\text{FF} = \frac{P_{\text{mpp}}}{J_{\text{sc}} V_{\text{oc}}} \tag{1.12}$$

is relatively high for both cases. Here, $P_{\text{mpp}}$ is the maximum power density that can be extracted from the device. Thus, the fill factor is understood as the largest

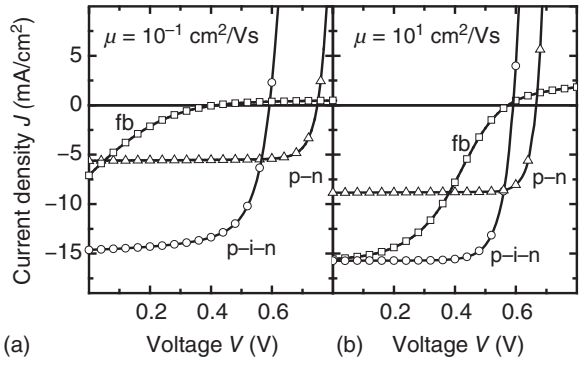


**Figure 1.7** Simulated current/voltage curves of the three solar-cell geometries introduced in Figure 1.6 for two charge carrier mobilities, namely, (a) $\mu = 10^{-1}\,\mathrm{cm^2/V\,s}$ and (b) $\mu = 10^{1}\,\mathrm{cm^2/V\,s}$. The main influence of a decreased mobility is a lower short-circuit current for the p–n-junction solar cell and a lower fill factor for the p–i–n-junction and the flatband solar cell, which feature voltage-dependent charge carrier collection.

rectangle that fits between a *J/V* curve and the axis divided by the rectangle with the sides $J_{sc}$ and $V_{oc}$.

For the p–n-junction solar cell, the open-circuit voltage also changes with mobility, which is due to increased surface recombination at high mobilities. This effect is pronounced in this simulation since the complete thickness of the absorber is rather thin (500 nm) and the surface recombination velocity is assumed to be rather high ($S = 10^5\,\mathrm{cm/s}$). The same effect also explains the relatively low short-circuit current density of the p–n-junction geometry since there is no built-in field or heterojunction that keeps the minorities away from the "wrong" contact (at $x = 500\,\mathrm{nm}$ in Figure 1.6). Thus, the p–n-junction solar cell is sensitive to the lack of selectivity of the back contact, that is, to surface recombination.

The p–i–n junction has a much higher short-circuit current density changing also very little upon decrease of mobility from $\mu = 10^1\,\mathrm{cm^2/V\,s}$ (Figure 1.7b) to $\mu = 10^{-1}\,\mathrm{cm^2/V\,s}$ (Figure 1.7a). However, the fill factor decreases because of the reduced capability of the device to collect all charge carriers when, under forward bias voltage, the built-in field is reduced (cf. Figure 1.6e). This phenomenon is called bias-dependent carrier collection. Furthermore, the open-circuit voltage of the p–i–n cell is lower than that of its p–n-type counterpart. Nevertheless, the p–i–n structure delivers the highest output power under the assumed, unfavorable conditions, namely, relative low carrier mobilities and high surface recombination velocities.

The flatband solar cell has the most remarkable *J/V* curves. The *J/V* curves in both mobility cases are partly bended, leading to extremely low fill factors. This so-called S-shaped characteristic becomes more pronounced in the low-mobility case. Note that, in practice, such behavior is common in devices with faulty contacts and consequently insufficient carrier separation capabilities.

### 1.2.5
### Nonradiative Recombination

The open-circuit voltage $V_{oc}$ of any solar cell is considerably lower than its radiative limit, implying that nonradiative recombination mechanisms like Auger recombination [12] or recombination via defects, which is usually called Shockley–Read–Hall recombination [13, 14], dominate real-world devices. Figure 1.8 compares the three main recombination mechanisms. In case of radiative recombination (Figure 1.8a), the excess energy of the recombining electron–hole pair is transferred to a photon. In case of (Figure 1.8b) Auger recombination [15, 16], the excess energy serves to accelerate a third charge carrier (electron or hole) which thermalizes rapidly by emitting phonons. The third recombination mechanism is Shockley–Read–Hall recombination via states in the forbidden gap. Here, the excess energy is also transferred to phonons, leading to an increase in the lattice temperature of the absorber.

In very-high-quality devices from monocrystalline silicon, the recombination will be limited by Auger recombination and surface recombination. This means that even with a perfect bulk material without any defects, recombination in an indirect semiconductor like silicon will most likely not be limited by radiative recombination. However, typical thin-film solar cells are made from amorphous or microcrystalline semiconductors that are far from defect-free. Here, the most important recombination mechanism is recombination via states in the forbidden gap. These states can be, for instance, due to defects like dangling bonds [17] or due to band tails [18–20] arising from disorder in the material. Especially in amorphous Si, there is not only a single state in the band gap as indicated in Figure 1.8c but a continuous distribution of states in energy. The theory and modeling of such defect distributions will be described later in Chapter 23, while we want to restrict ourselves here to some simple examples with a single defect state.

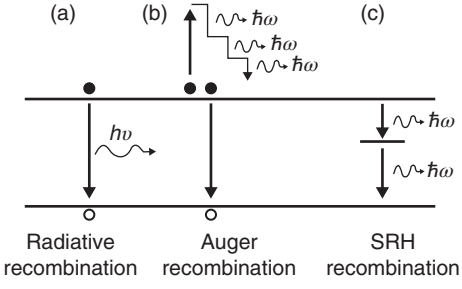


**Figure 1.8** Overview over the three basic recombination mechanisms for photogenerated excess carriers in a semiconductor. The excess energy is either transferred to (a) a photon, (b) kinetic energy of an excess electron or hole, or (c) phonons. For case (b), in the so-called Auger recombination, the kinetic energy of the electron is lost by collisions with the lattice, which heats up. In case (c), the emission of phonons becomes possible by the existence of states in the forbidden gap. This recombination mechanism is called Shockley–Read–Hall recombination.

To visualize the influence of increased recombination rates on the current/voltage curve of solar cells, we made some numerical simulations using a very simple model for recombination. This model assumes recombination via a defect in the middle of the forbidden gap, assuming equal capture cross sections $\sigma$ for electrons and holes. Then the recombination rate according to Shockley–Read–Hall statistics is

$$R = \frac{np - n_i^2}{(n+p)\tau}, \tag{1.13}$$

where $\tau$ is called the lifetime of the charge carrier. This lifetime depends on the density $N_T$ of defect states, the capture cross section $\sigma$, and the thermal velocity $v_{th}$ via

$$\tau = (v_{th}\sigma N_T)^{-1}. \tag{1.14}$$

Figure 1.9 shows the current/voltage curves of a (a) p–i–n-junction solar cell and (b) a p–n-junction solar cell for a constant mobility $\mu = 1\,\mathrm{cm}^2/\mathrm{V\,s}$ (for electrons and holes) and with a varying lifetime $\tau = 1\,\mathrm{ns}$, 10 ns, 100 ns, 1 µs, and 10 µs. All other parameters are defined in Table 1.1. It is important to note that a reduction of the lifetime has a different influence on the two geometries, which is in accordance with what we already observed when varying the mobility. For p–i–n-junction solar cells, a decrease of the lifetime leads to a decrease in open-circuit voltage, in fill factor, and in short-circuit current density. In contrast, the p–n-junction solar cell does not suffer from a decreased fill factor. The shape of the *J/V* curves stays practically the same. For low lifetimes (and/or low mobilities), the charge carrier collection in p–i–n-junction solar cells is

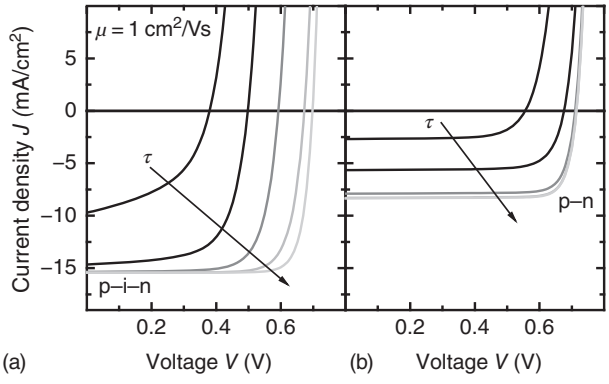


**Figure 1.9** Current/voltage curves of (a) a p–i–n-junction solar cell and (b) a p–n-junction solar cell for a constant mobility $\mu = 1\,\mathrm{cm}^2/\mathrm{V\,s}$ (for electrons and holes) and with a varying lifetime $\tau = 1\,\mathrm{ns}$, 10 ns, 100 ns, 1 µs, and 10 µs. All other parameters are defined in Table 1.1. An increasing lifetime helps to increase $V_{oc}$ in both cases up to the level defined by surface recombination alone. In case of the p–i–n-junction solar cell, the *FF* increases as well.

**Table 1.1** Summary of all parameters for the simulations in this chapter that are not changed for the simulation.

| Parameters for all simulations in this chapter | Values |
|---|---|
| Band gap $E_g$ (eV) | 1.2 |
| Effective density of states $N_C$, $N_V$ for conduction and valence band ($cm^{-3}$) | $10^{20}$ |
| Doping concentrations $N_D$, $N_A$ in all doped layers of p–n- and p–i–n-junction solar cells ($cm^{-3}$) | $10^{19}$ |
| Total thickness $d$ (nm) | 500 |
| Generation rate $G$ ($cm^{-3}\,s^{-1}$) | $2\times10^{21}$ |
| Surface recombination velocity $S$ (cm/s) | $10^5$ |

The mobilities and lifetimes, which are changed, are always given in the respective figure captions.

voltage dependent. For p–n-junction solar cells, this is not the case. But apart from the influence the carrier lifetime has on charge extraction, which is very similar to the effect of the mobility, the lifetime has a pronounced influence on the open-circuit voltage. The increase of $V_{oc}$ with increasing lifetime $\tau$, however, seems not to follow a simple relation. For high values of $\tau$, $V_{oc}$ saturates for both p–i–n-junction and p–n-junction solar cells. This saturation is due to surface recombination, which limits the maximum attainable open-circuit voltage $V_{oc}$.

## 1.3 Functional Layers in Thin-Film Solar Cells

Until now, we have discussed the photovoltaic effect, the requirements for the material properties to come close to a perfect solar cell, and the possible geometries to separate and extract charge carriers. In typical crystalline silicon solar cells, nearly all of these requirements and tasks have to be fulfilled by the silicon wafer itself. Charge extraction is guaranteed by diffusing phosphorus into the first several hundred nanometers of the p-type wafer to create a p–n junction. The wafer is texture etched to obtain a light-trapping effect and to decrease the reflection at the front surface. The only additional layers that are necessary are the metal grid at the front, an antireflective coating (typically from $SiN_x$), and the metallization at the back.

Thin-film solar cells are usually more complex devices with a higher number of layers that are optimized for one or several purposes. In general, there are two configurations possible for any thin-film solar cell as shown in Figure 1.10. The first possibility is that light enters the device through a transparent superstrate.

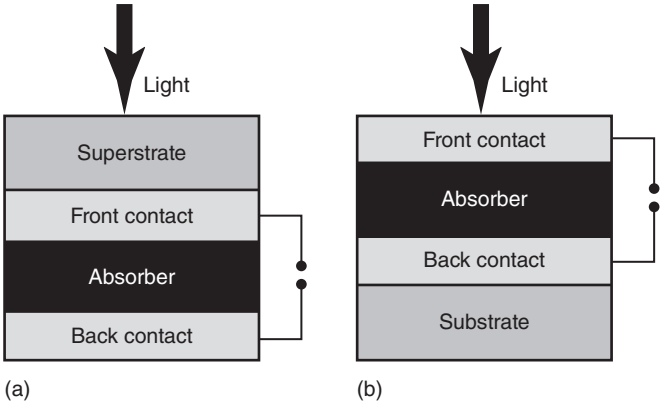


**Figure 1.10** Sketch of the layer sequences to build up the system for thin-film solar cells in superstrate (a) and substrate configuration (b). The minimum number of layers in excess of the supporting sub- or superstrate consists of the transparent and conductive front contact, the absorber layer, and the back contact.

**Table 1.2** List of the four types of layers in a thin-film solar cell together with their specific tasks and requirements necessary for an efficient solar cell.

| Layer type | Possible tasks and requirements |
|---|---|
| Substrate/superstrate | Mechanical and thermal stability, transparency (superstrate) |
| Front contact | Light trapping, antireflection, electrical contact, charge extraction |
| Absorber | Absorb light, charge extraction, low recombination |
| Back contact | Light trapping, high reflection, electrical contact, charge extraction |

The superstrate has to maintain the mechanical stability of the device while at the same time being extremely transparent. The superstrate is followed by layers which are part of the front contact, followed by the absorber layer and the layers that form the back contact. The second possibility is to inverse the layer stack, starting with the front contact, the absorber, and the back contact. These layers are all deposited on top of a substrate. Because light does not have to pass the substrate to enter the solar cell, the substrate can be transparent or opaque.

Table 1.2 summarizes the roles and the requirement for the three functional layers and the substrate or superstrate of thin-film solar cells. The substrate or superstrate provides mechanical stability. The functional layers are deposited onto the substrate or superstrate; thus, it has to be thermally stable up to the highest temperature reached during the complete deposition process.

The front contact and back contact layers have to provide the electrical contact of the solar cell to the outside world, that is, the layers need high conductivities and must make a good electric contact to the absorber layers. In addition, the built-in field required for efficient charge extraction (especially at higher voltage bias) of a p–i–n junction as depicted in Figure 1.6 requires doped contact layers. In devices that require efficient light trapping, usually the front and/or back contact layers are textured and have a lower refractive index than the absorber layer. Thus, the front contact layer additionally serves as an internal antireflective coating. In addition, a possible texture of the contact/absorber interface will lead to scattering of light and to increased path lengths of weakly absorbed light in the absorber layer. The back contact should have a high reflectivity so that weakly absorbed light is reflected multiple times.

The absorber layer is central to the energy conversion process, requiring a steep rise of the absorption coefficient above the band gap, a high mobility and low recombination rates for efficient charge collection, and a high open-circuit voltage potential. In case of a p–n-junction device, the absorber layer must be moderately doped either intentionally or by intrinsic doping due to defects. In case of a p–i–n-junction device, the main absorber layer, the i-layer, should be undoped.

## 1.4 Comparison of Various Thin-Film Solar-Cell Types

The basic schemes of the layer stack of a thin-film solar cell, as presented in Figure 1.10, are implemented in different ways in the different thin-film technologies. In the following, we will briefly discuss the main characteristics of the thin-film technologies that appear in examples in this book. These technologies are the $Cu(In,Ga)Se_2$ solar cell, the CdTe-based solar cell, the kesterite $Cu_2ZnSn(S,Se)_4$ solar cell, the thin-film silicon solar cell with amorphous and microcrystalline silicon absorbers, the perovskite solar cell, and the organic solar cell. We also discuss the main challenges in future developments and how characterization of materials and devices can help to improve the devices. For those readers who desire a more detailed insight in the physics and technology of the different thin-film solar cells, we refer to a number of books and review articles on the topic. The physics and particularly the fabrication of all types of thin-film solar cells are discussed in Refs [21–23], the physics of Cu-chalcopyrite solar cells in Refs [24, 25], the interfaces of CdS/CdTe solar cells in Ref. [26], the physics of amorphous hydrogenated silicon in Ref. [27], the physics and technology of thin-film silicon solar cells in Refs [28–32], the aspect of charge transport in disordered solids in Ref. [33], kesterite-type solar cells in Refs [34, 35], perovskite solar cells in Refs [36, 37], and organic solar cells in Ref. [38].

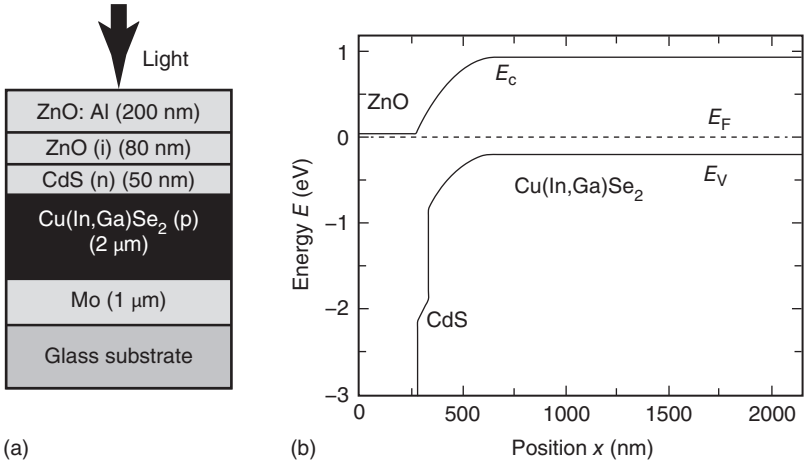


**Figure 1.11** (a) Layer-stacking sequence and (b) energy band diagram of a typical ZnO/CdS/Cu(In,Ga)$Se_2$ heterojunction solar cell.

### 1.4.1 Cu(In,Ga)$Se_2$

#### 1.4.1.1 Basic Properties and Technology

Solar cells with an absorber layer made from Cu(In,Ga)$Se_2$ are currently the state of the art of the evolution of Cu-based chalcopyrites for use as solar cells. Heterojunctions between CdS and $Cu_2S$ were the basis for first approaches for thin-film solar cells since the 1950s [39–42]. In 1974 first work on the light emission and light absorption of CdS/$CuInSe_2$ diodes was published [43–45]. While $CuInSe_2$ was not further considered for applications as a near-infrared light-emitting diode (LED), its high absorption coefficient and its electronically rather passive defects make it a perfect choice for use as a microcrystalline absorber material. Inclusion of Ga atoms on the In lattice site such that the ratio of [Ga]/([Ga] + [In]) becomes around 20% shifts the band gap from 1.04 eV to around 1.15 eV, which is nearly perfect for a single-junction cell (cf. Figure 1.3). Today, thin-film solar cells with a Cu(In,Ga)$Se_2$ absorber layer are the most efficient thin-film technology with laboratory efficiencies up to 21.7% [46].

The classical layer stack for this type of solar cell is shown in Figure 1.11a. It consists of a typically 1 μm thick Mo layer deposited on a soda-lime glass substrate and serving as the back contact for the solar cell. Then, Cu(In,Ga)$Se_2$ is deposited on top of the Mo back electrode as the photovoltaic absorber material. This layer has a thickness of 1–2 μm. The heterojunction is then completed by chemical bath deposition of CdS (typically 50 nm) and by the sputter deposition of a nominally undoped (intrinsic) i-ZnO layer (usually of thickness 50–70 nm) and then a heavily doped ZnO:Al window layer.

The Cu(In,Ga)$Se_2$ absorber material yielding the highest efficiencies is prepared by coevaporation from elemental sources. The process requires a maximum

substrate temperature of ~550 °C for a certain time during film growth, preferably toward the end of growth. Advanced preparation sequences always include a Cu-rich stage during the growth process and end up with an In-rich overall composition in order to combine the large grains of the Cu-rich stage with the otherwise more favorable electronic properties of the In-rich composition. The first example of this kind of procedure is the so-called Boeing or *bilayer process* [47] which starts with the deposition of Cu-rich $Cu(In,Ga)Se_2$ and ends with an excess In rate to achieve a final composition that is slightly In poor. The most successful coevaporation process is the so-called three-stage process [48] where first $(In,Ga)_2Se_3$ (likewise In, Ga, and Se from elemental sources to form that compound) is deposited at lower temperatures (typically around 300 °C). Then Cu and Se are evaporated at an elevated temperature and finally again In, Ga, and Se to ensure the overall In-rich composition of the film even if the material is Cu rich during the second stage.

The second class of absorber preparation routes is based on the separation of deposition and compound formation into two different processing steps. High efficiencies are obtained from absorber prepared by selenization of metal precursors in $H_2Se$ [49] and by rapid thermal processing of stacked elemental layers in a Se atmosphere [50]. These sequential processes have the advantage that approved large-area deposition techniques such as sputtering can be used for the deposition of the materials. The $Cu(In,Ga)Se_2$ film formation then requires a second step, the selenisation step typically performed at similar temperatures as the coevaporation process. Both absorber preparation routes are now used in industrial application.

Important for the growth of the $Cu(In,Ga)Se_2$ absorber is the active role of Na during absorber growth. In most cases, the Na comes from the glass substrate and diffuses into the absorber [51]. But there are also approaches where Na is incorporated by the use of Na-containing precursors [52, 53]. The explanations for the beneficial impact of Na are manifold, and it is most likely that the incorporation of Na in fact results in a *variety* of consequences (for a review see Ref. [54]).

#### 1.4.1.2 Layer-Stacking Sequence and Band Diagram of the Heterostructure

Figure 1.11 displays the layer-stacking sequence (a) and the band diagram of the $ZnO/CdS/Cu(In,Ga)Se_2$ heterojunction (b). The back contact consists of a sputtered Mo layer. In excess of producing a functional, conductive contact, proper preparation of this layer is also important for adhesion of the absorber film and, especially, for the transport of Na from the glass substrate through the Mo layer into the growing absorber. A homogeneous and sufficient supply of Na depends much on the microstructure of this layer. In contrast, if Na is supplied from a precursor, additional blocking layers prevent out-diffusion of Na from the glass. Quantitative chemical depth profiling as described in Chapter 19 is a decisive tool to shed more light into the role of Na and on its way how it is functional during absorber growth.

The $Cu(In,Ga)Se_2$ absorber material grown on top of the Mo contact is slightly p-type doped by native, intrinsic defects, most likely Cu vacancies [55]. However, the net doping is a result of the difference between the acceptors and an almost

equally high number of intrinsic donors [56, 57]. Thus, the absorber material is a highly compensated semiconductor. Furthermore, the material features electronic metastabilities like persistent photoconductivity [58] which are theoretically explained by different light-induced defect relaxations [59]. However, final agreement on the observed metastability phenomena has not yet achieved, leaving an urgent need for further theoretical and experimental access to the complex defect physics of $Cu(In,Ga)Se_2$ (for a review of the present status, see Ref. [48]). Some experimental and theoretical methods helpful for further research are outlined in Chapters 11 and 21 of the present book.

Another puzzle is the virtual electronic inactivity of most grain boundaries in properly prepared polycrystalline $Cu(In,Ga)Se_2$ absorbers being one essential ingredient for the high photovoltaic efficiencies delivered by this material. A discussion of the present status is given in Ref. [60]. A great part of the structural analysis methods discussed in the present book (Chapters 13–15 and 17) describes tools indispensable for a better understanding of the microstructure of the $Cu(In,Ga)Se_2$ absorber material.

The surface properties of $Cu(In,Ga)Se_2$ thin films are especially important, as this surface becomes the active interface of the completed solar cell. The free surface of as-grown $Cu(In,Ga)Se_2$ films exhibits a very unique feature, namely, a widening of the band gap with respect to the bulk of the absorber material [61, 62]. This band-gap widening results from a lowering of the valence band and is effective in preventing interface recombination at the absorber–buffer interface [63, 64]. This surface layer has an overall Cu-poor composition and a thickness of 10–30 nm [65]. Understanding the interplay between this surface layer and the subsequently deposited buffer layer is one of the decisive challenges for the present and future research.

The 50 nm thick CdS buffer layer is in principle too thin to complete the heterojunction. In fact the role of the CdS buffer in the layer system is still somewhat obscure. It is however clear that the undoped (i) ZnO layer is also a vital part of a successful buffer/window combination. Furthermore, both interfaces of the CdS interlayer to the $Cu(In,Ga)Se_2$ absorber and to the (i) ZnO play a vital role [66]. Under standard preparation conditions, the alignment of the conduction bands at both interfaces is almost flat [67] such that neither barrier for electron transport occurs nor is the band diagram distorted in a way to enhance interface recombination. However, it turns out that a replacement of CdS by a less cumbersome layer is not straightforward. Though, while promising materials like In(OH,S), Zn(OH,S), $In_2Se_3$, ZnSe, and ZnS (for an overview see Ref. [68]) mostly in combination with standard ZnO double layer have been investigated in some detail, no conclusive solution has been found despite reported efficiencies of 18% using ZnS buffer layers [69]. Recent research [70] focuses at combinations of Zn(S,O,OH)/ZnMgO replacing the traditional CdS/(i) ZnO combination. Alternative buffer layers like ZnS also have the advantage of a higher band-gap energy $E_g = 3.6$ eV compared to that of CdS $E_g = 2.4$ eV. By the higher $E_g$, parasitic absorption in the buffer layer is restricted to a much narrower range, and the short-circuit current density in Cd-free cells can exceed that of standard devices by up to 3 mA/cm$^2$ [63]. However, all

technological improvements rely on our scientific understanding of the physics, chemistry, and microstructure of the heterointerfaces involved in the solar cell. Surface analysis methods as those discussed in Chapters 18 and 19 have already contributed much to our present knowledge and provide the promise to deepen it further.

## 1.4.2 CdTe

### 1.4.2.1 Basic Properties and Technology

Just as the CdS/Cu(In,Ga)$Se_2$ solar cell, also the CdS/CdTe devices are descendants of the first CdS/$Cu_2S$ solar cells. In the mid-1960s, first experiments with tellurides were performed. Efficiencies between 5 and 6% were obtained for CdTe/$CuTe_2$ devices [71, 72]. Since Cu diffusion led to instabilities in these devices, instead, CdS and CdTe were combined to form a p–n heterojunction with efficiencies around 6% [73]. Thirty years later, the efficiency has increased to more than 21% [74]. In addition, CdTe solar modules represent the by far most successful photovoltaic thin-film technology with a share of about 10% in the global photovoltaic market (data from 2014) [75].

One decisive reason for this success is the relatively ease with which CdTe solar cells and modules are prepared. Several types of transparent conductive oxides (TCO) are used as front contact materials for preparation of CdTe solar cells, $SnO_2$:F and $In_2O_3$:F being the most common ones. Both materials, CdS and CdTe, forming the heterojunction of the solar cell, are grown with similarly fast and reliable methods, including closed-space sublimation, spraying, screen printing followed by sintering, and electrodeposition. Since CdS grows natively as n-type material and CdTe as p-type material, the p–n heterojunction forms automatically.

However, in order to improve the device efficiency substantially, an additional step, the $CdCl_2$ activation, is necessary. A vapor-based approach is most useful with regard to industrial applications [76]. The activation step leads to an intermixing of CdS and CdTe close to the heterointerface and to the formation of a Cu(Te,S) compound. In some cases, recrystallization of the CdTe film was observed after $CdCl_2$ treatment [77]. In any case, the intermixing process is decisive for the improvement of the device performance.

The major challenge for reliable manufacture of efficient devices is to produce a stable and ohmic back contact to the CdTe absorber with its high electron affinity. Often, back contacts are made with materials that contain Cu, such as $Cu_2Te$, ZnTe:Cu, or HgTe:Cu, enabling a relatively low contact resistance. However, Cu diffusion in CdTe is fast and extends deeply into the absorber, thereby affecting considerably the stability of the device [78]. Cu-free alternative contact materials include embrace, for example, $Sb_2Te_3$ [79]. Often, an etching step is used to produce a Te-rich interlayer, providing higher p-type doping and, consequently, a reasonably low-ohmic contact [80]. Recently, substantial advances in photovoltaic

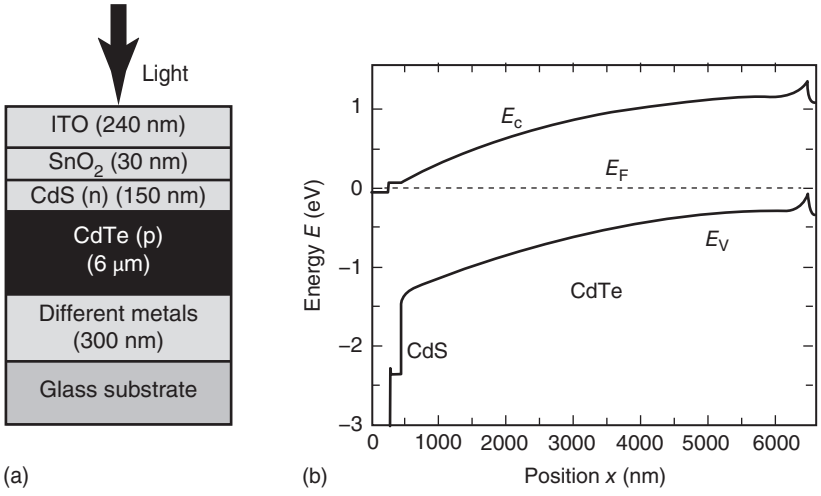


**Figure 1.12** (a) Layer-stacking sequence and (b) energy band diagram of a typical CdTe-based solar cell following Ref. [82].

performance have been achieved by doping of the CdTe absorber [81] layer as well as by introducing compositional gradients.

#### 1.4.2.2 Layer-Stacking Sequence and Band Diagram of the Heterostructure

From the point of view of the layer-stacking sequence and the band diagram shown in Figure 1.12a and b, the CdS/CdTe heterostructure is quite similar to those of the CdS/Cu(In,Ga)$Se_2$ heterostructure given in Figure 1.11. One obvious difference is the low doping density of the CdTe absorber, making the device somewhat a hybrid between a p–i–n and a p–n junction. The built-in field almost stretches from the heterointerface toward the back contact. As we have already seen, such a configuration is helpful for carrier collection but has the drawback of delivering lower open-circuit voltages than a p–n-type device with a relatively narrow space charge region if the density of recombination active defects doesn't depend on the doping concentration.

The band diagram at the back contact features a highly p-doped region due to Cu indiffusion or due to the formation of a Te-rich interlayer. This leads to a relatively thin yet high barrier for holes. Thus, the electrical contact is achieved via tunneling from the absorber into the back metal. The modeling of CdTe solar cells, including a proper approach to the back contact, which usually is by far not perfectly ohmic, represents a major challenge as discussed in Chapter 23.

The average grain sizes in the polycrystalline CdTe absorbers range from 1 to 2 mm, thus somewhat larger than in Cu(In,Ga)$Se_2$. However, the grain boundaries are considerably more electronically active than in Cu(In,Ga)$Se_2$. For instance, photocurrent concentration along grain boundaries [83] indicates type inversion of grain boundaries in CdTe. This could be helpful for current collection (along the grain boundaries) but also implies losses in open-circuit voltage. Again, connecting microstructural analysis with highly resolved measurements of electronic

properties by scanning techniques as described in Chapters 13 and 14 will clarify the picture in the future.

The favorable flat conduction-band alignment at the CdTe/CdS as well as at the CdS/TCO interface as featured by Figure 1.12b is similar to the situation for $Cu(In,Ga)Se_2$ devices. In CdTe solar cells this is basically a result of the $CdCl_2$ activation process and of intermixing [73].

### 1.4.3
### $Cu_2ZnSn(S,Se)_4$

Photovoltaic devices with same thin-film stacking sequences as for $Cu(In,Ga)Se_2$ solar cells but replacing In and Ga in the absorber layer by the earth-abundant elements Zn and Sn have been developed during recent years as cost-effective alternatives. The tetragonal crystal structure of the compound $Cu_2ZnSn(S,Se)_4$, of kesterite type, is similar to the chalcopyrite-type structure of $Cu(In,Ga)Se_2$ [84]. A Cu/Zn disorder (referred to as "disordered kesterite") causes a high concentration of $Cu_{Zn}$ and $Zn_{Cu}$ antisite defects [76]. In the material system $Cu_2ZnSn(S,Se)_4$, it is possible to obtain band-gap energies of the compound semiconductors ranging from 1.0 to 1.5 eV by varying the [S]/([S] + [Se]) ratio from 0 to 1 [85]. Power-conversion efficiencies of 8.4% [86], 9.2% [87], and 12.6% [88] have been achieved by using $Cu_2ZnSn(S,Se)_4$ absorber layers with [S]/([S] + [Se]) ratios of 1 ($Cu_2ZnSnS_4$), 0 ($Cu_2ZnSnSe_4$), and about 0.25.

Since, according to the available phase diagrams [89, 90], the kesterite phase of $Cu_2ZnSn(S,Se)_4$ exhibits a small existence region with 1–2 at.% deviation in the composition at most growth temperatures of around 550 °C [35], secondary phases can be expected to be present when synthesizing $Cu_2ZnSn(S,Se)_4$ bulk crystals or thin films. Of the possible secondary phases, $Cu_2(S,Se)$, Zn(S,Se), Sn(S,Se), $Sn(S,Se)_2$, and $Cu_2Sn(S,Se)_3$ were reported to be most likely [91]. Some of these compounds can be considered to affect collection of charge carriers as well as radiative recombination in the photovoltaic devices [85]. However, recombination at the $CdS/Cu_2ZnSn(S,Se)_4$ interface was identified to influence the device performance more dominantly, probably due to a cliff-like conduction-band alignment in the solar cells with S-containing absorber layers. Therefore, further improvement of the power-conversion efficiencies to above 13% may be achieved by reducing this interface recombination [80], for example, by application of buffer layers other than CdS, or by reducing the density of secondary phases at this interface.

### 1.4.4
### Thin-Film Silicon Solar Cells

#### 1.4.4.1 Hydrogenated Amorphous Si (a-Si:H)

Central to the working principle of semiconductors is the forbidden energy gap derived from the periodicity of the crystal lattice. However, it is exactly this

strict periodicity that is lacking in amorphous semiconductors, which have a short-range order but no long-range order as their crystalline counterparts. The structural disorder caused by variations in bond lengths and angles has several implications for the electronic and optical properties of amorphous materials. The most important feature is the peculiar density of electronic states in amorphous silicon featuring localized states close to the band edges that arise from disorder and a distribution of deep states due to unpassivated, that is, dangling, bonds. In addition the word band gap is no longer adequate in amorphous semiconductors. Instead, an optical gap is defined from the onset of absorption, while a mobility gap is defined as the approximate demarcation line between localized and extended states [92]. Despite the fact that the mobility gap is not a forbidden zone for electrons but instead full of localized states, amorphous silicon still proves to be a useful material for thin-film devices like solar cells, photodetectors, and transistors [93].

While first crystalline silicon solar cells with reasonable efficiencies of about $\eta = 6\%$ were already developed in 1954 [94], the research on amorphous silicon first needed two breakthroughs before the fabrication of the first amorphous silicon solar cells in 1976 became possible [95]. The first breakthrough was the realization that the addition of considerable amounts of hydrogen helped to passivate dangling bonds in the amorphous material thereby leading to sufficiently low defect densities that hydrogenated amorphous silicon showed some of the important characteristics of useful semiconductors like dopability and photoconductivity [96]. The second breakthrough was the successful doping of amorphous silicon [97].

Despite the defect passivation with hydrogen, the defect densities in a-Si:H are still relatively high with diffusion lengths between 100 and 300 nm [98]. In doped a-Si:H layers, the defect density is two or three orders of magnitude higher, and the diffusion length is accordingly even lower. Thus, a p–n junction as used in crystalline silicon but also in Cu(In,Ga)$Se_2$ solar cells would not work for a-Si:H, since the diffusion length is too low. Because the absorber thickness cannot be made much thinner than the diffusion length due to the large losses because of insufficient light absorption, a p–i–n-junction configuration has to be used. The first advantage is that most of the absorber layer consists of intrinsic a-Si:H with its higher carrier lifetime than doped a-Si:H. The second advantage is that the built-in field helps with extracting charge carriers as shown in Figure 1.13. The advantage of the p–i–n configuration is that electron and hole concentrations are similar in a relatively large portion of the absorber volume, which increases defect recombination, which is automatically highest, when electron and hole concentrations are approximately equal.

Figure 1.13 shows the typical layer stack and band diagram of an a-Si:H p–i–n-type solar cell. Usually a superstrate configuration is used, although a substrate configuration is also possible. In the latter case, the solar cell is deposited on the substrate starting with the back contact and the n-type layer. Thus, such a solar cell is called nip solar cell, in which n–i–p represents the deposition order. In both cases of a substrate or superstrate configuration, the illumination is always from the p side. This is due to the lower mobility of holes in a-Si:H. It is therefore

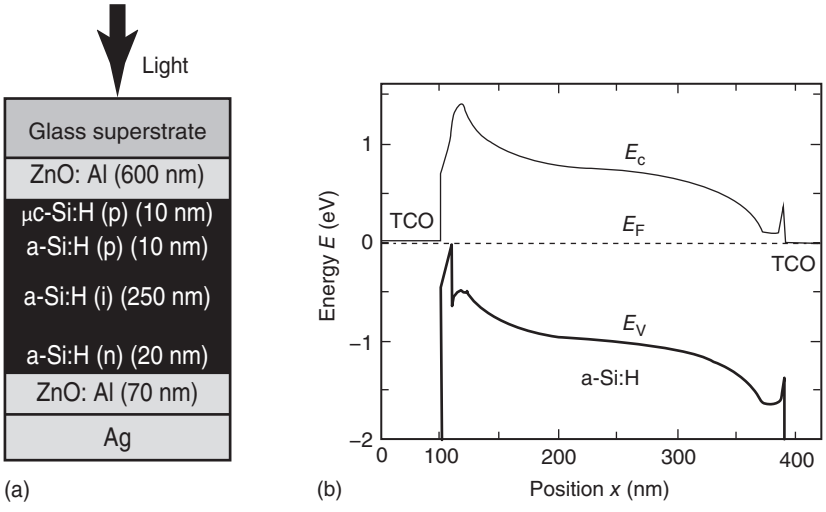


**Figure 1.13** (a) Stacking sequence and (b) band diagram of a typical a-Si:H p–i–n solar cell. The main absorber layer is intrinsic, while the built-in field is due to the thin doped silicon layers. Due to the asymmetric mobilities between electrons and holes, the p-type layers will always be on the illuminated side, ensuring that the holes with their lower mobility have the shorter way to the contacts.

beneficial to have the hole contact on the illuminated side, where the generation rate is higher. With the hole contact on the illuminated side, the distance the slowest carrier has to travel to the contacts is minimized.

#### 1.4.4.2 Metastability in a-Si:H: The Staebler–Wronski Effect

Shortly after the first reports on a-Si:H solar cells, Staebler and Wronski [99] published their findings on metastability in a-Si:H. Under illumination the conductivity of a-Si:H degrades but can be restored by annealing at temperatures of about 425 K. This degradation effect is known as the Staebler–Wronski effect. The metastable behavior is ascribed to the light-induced creation of additional defects. It is generally accepted that these metastable defects are additional dangling bonds that act like recombination centers in the material and that these dangling bonds are created by the breaking of weak or strained Si–Si bonds. Hydrogen plays an important role in the metastable behavior of a-Si:H; however, there is no consensus on the exact mechanisms involved and the role of hydrogen in the Staebler–Wronski effect [100–103]. The creation of additional recombination centers affects a-Si:H-based solar cells to such a degree that the Staebler–Wronski effect is a severe limitation for the application of a-Si:H in single-junction solar cells.

#### 1.4.4.3 Hydrogenated Microcrystalline Silicon (μc-Si:H)

As can be seen by comparison with Figure 1.3b, the high optical gap of a-Si:H of approximately 1.75 eV (the exact value depending on the definition and on the hydrogen content) is too high for a single-junction solar cell. It was therefore

an important discovery in thin-film silicon solar-cell research to find a way to prepare hydrogenated microcrystalline silicon (μc-Si:H) with approximately the same band gap as crystalline silicon ($E_g$ (c-Si) = 1.12 eV) that had a sufficient quality for use in solar cells. First μc-Si:H layers were deposited in the 1960s [104], and successful doping was achieved in the 1970s [105]. However, the material had insufficient electronic quality for use in solar cells. The use of gas purifiers in the 1990s by the Neuchâtel group made the fabrication of μc-Si:H layers with sufficiently low oxygen contents [106–108] and the successful fabrication of first μc-Si:H solar cells with reasonable efficiencies possible [109, 110].

#### 1.4.4.4 Micromorph Tandem Solar Cells

One possibility to overcome [111] the efficiency limit of Shockley and Queisser is the use of a multijunction solar cell with absorber layers having different band gaps. The highest band-gap absorber should be on the illuminated side such that all high-energy photons are absorbed by the absorber with the higher band gap and the low-energy photons are absorbed by the cell or the cells with the lower band gap(s). If every absorber has its own p–n junction or p–i–n junction, then they can be deposited on top of each other such that one obtains two or more series connected solar cells on top of each other. This approach minimizes the losses due to thermalization of carriers and due to the transparency of any solar cell for photons with energies below the band gap of the absorber. With a similar approach as discussed in Section 1.2.1, the efficiency [112] and the optimal band-gap combinations can be calculated for multijunction solar cells in general and tandem (i.e., two-junction solar cells) in particular [113, 114]. It is a fortunate coincidence that the optimum combination for a tandem solar cell is close to the actual band gaps of amorphous ($E_g$ (a-Si:H) ≈ 1.75 eV) and microcrystalline silicon ($E_g$ (μc-Si:H) ≈ 1.2 eV). Although in principle efficiencies above the SQ limit for single-junction solar cells are possible with such a configuration, in reality the efficiencies are much lower than the SQ limit and even lower than efficiencies of real crystalline Si single-junction solar cells. Nevertheless, the tandem cell made from a-Si:H and μc-Si:H has achieved slightly higher efficiencies than either of the single-junction devices (see Ref. [29] for an overview). For these thin-film tandem cells with their relatively low mobilities, a second motivation arises for the use of tandem solar cells. Since the built-in field decreases for increasing thickness and since the charge collection becomes increasingly difficult with increasing distance to the contacts, thin solar cells have higher fill factors than thicker solar cells. The tandem approach is a useful way to keep individual cell thicknesses low and at the same time have a higher total thickness and a better absorptance.

#### 1.4.4.5 Liquid-Phase Crystallized Si

Recently, substantial progress has been demonstrated in the development of polycrystalline Si solar cells on glass substrates. The defect concentration in the Si absorber layer, one of the main reasons for the so far limited device performance

(power-conversion efficiency of about 10%), has been reduced considerably by replacing the state-of-the-art solid-phase crystallization of the Si precursor layer by a laser-beam liquid-phase crystallization (LPC) process [115, 116]. This synthesis step can lead to large average grain sizes of several hundreds of micrometers, similar to those of multicrystalline Si wafers. As a result, the open-circuit voltage has increased to more than 650 mV, and power-conversion efficiencies of well above 11% have been demonstrated [117]. Solar cells based on LPC-Si thin films on glass substrates may emerge as low-cost alternatives to multicrystalline wafer-based Si solar cells, provided that light incoupling and contacting in the solar-cell stack can be further optimized.

### 1.4.5
### Metal-Halide Perovskite Solar Cells

Semiconducting perovskites with one organic and one inorganic cation and three halogen atoms as anions were initially tested as dyes in DSSCs. The initial results were hardly promising in terms of stability, because the liquid electrolyte was quickly dissolving the perovskite layer [118]. However, once the liquid electrolyte was replaced by an organic hole transport layers, solar-cell efficiencies and stability were quickly improving. However, the stability still remains on a low level compared with inorganic materials. After it had become apparent that the most frequently used material $CH_3NH_3PbI_3$ was perfectly capable of light absorption as well as electron and hole collection [119], a large variety of device designs became possible, going way beyond the initial use in "DSSCs" with solid-state electrolytes.

$CH_3NH_3PbI_3$ exhibits an absorption coefficient similarly high as the one of $Cu(In,Ga)Se_2$ or GaAs and therefore can reach high photocurrent densities for rather low thicknesses [120]. The band-gap energy of $CH_3NH_3PbI_3$ is around 1.6 eV, that is, it is slightly too high for a single-junction device but close to the ideal band-gap energy for a tandem solar cell. The high conversion efficiencies [121] reached for a thin-film photovoltaic material with a band-gap energy as high as 1.6 eV make the perovskites rather unique, because of their use for tandem solar cells which has previously been possible only for the family of III – V semiconductors and by fabricating a-Si:H/μc-Si:H stacks. Charge carrier lifetimes in the material are frequently reported to exceed 100 ns, which is an excellent value for a polycrystalline semiconductor. Mobilities reported in the literature, however, vary from values around 100 $cm^2/V\,s$ for single crystals to values between $10^{-3}$ [122] and 10 $cm^2/V\,s$ [123] for thin films. Especially because the mobility values at the lower end of the spectrum of reported values belong to highly efficient devices with efficiencies approaching 20% [122], the understanding and measurement of charge transport properties seem to be currently a mostly unresolved challenge.

A major reason for the success but also some associated peculiarities of $CH_3NH_3PbI_3$ seems to be based on the defect physics of the material [124]. Due to the three lattice positions of the perovskite crystal ($ABX_3$), there are 12 possible

intrinsic defects, most of which are shallow in the case of $CH_3NH_3PbI_3$, doping the device rather than leading to recombination centers. The few deep defects exhibit large formation enthalpies and occur therefore less frequently than in many other polycrystalline materials. Nevertheless, the low concentration of deep defects still seems to control charge carrier recombination, which becomes apparent from the LED quantum efficiencies of LEDs being much smaller than one [125]. The shallow defects which are doping the device are able to diffuse through the device [126], thereby leading to a doping profile that is not constant as a function of time and bias voltage. This leads to hysteresis effects in the current/voltage curves, that is, depending on the voltage sweep direction and the speed of the voltage sweep, different efficiencies are measured [127].

While the efficiency of perovskite solar cells has recently surpassed 20% [121], future research efforts are likely directed toward topics such as improved long-term stability, reproducibility of device fabrication routines, alternatives for Pb as the inorganic cation [128], and the use of perovskites in tandem cells.

### 1.4.6 Organic Solar Cells

There exist a wide variety of solar cells that exploit the high absorption coefficients of organic molecules and use heterojunctions to cope with the high binding energies in these molecules. The most relevant among them are DSSCs [129], polymer–fullerene solar cells [130], small-molecule [131] solar cells, and polymer–nanoparticle solar cells [132]. DSSCs use the organic molecule as absorber, an inorganic mesoporous scaffold (typically $TiO_2$) as electron transporter, and a liquid- or solid-state electrolyte to transport the positive charge (a hole or an ion).

A second option is to merge the functions of absorption and transport of one charge carrier to produce a solar cell made up of two different types of materials, usually termed electron donor and electron acceptor. The electron donor may be a polymer or a highly absorbing small molecule. Originally, polymers were more widely used because they are solution processable (in contrast to many small molecules) and therefore do not require expensive equipment for solar-cell fabrication. However, nowadays, also solution-processable small molecules are used as electron donors [133], in addition to the classical concept of using evaporated small molecules.

The electron acceptor is typically a fullerene. In combination with solution-processable small molecules, fullerenes with side chains are used which are designed to improve the solubility of the fullerene. This allows for mixing the donor and the fullerene in solution and then spin coating or doctor blading the ink on a substrate. In the case of donor materials that have to be evaporated, usually pure $C_{60}$ (without any side chains) is used and evaporated as well. Alternatives for fullerenes are other small molecules or polymers as well as inorganic nanoparticles. None of these concepts have so far been used in the highest

efficient devices. However, especially in the case of nonfullerene small-molecule acceptors, promising efficiencies have already been reached [134].

Independent of which material combination is used, the two types of materials are usually intimately mixed to form a so-called bulk heterojunction. The term bulk heterojunction implies that the bulk of the material consists of a blend of two different molecules or nanoparticles mixed so intimately that any point in the volume is "close" to a heterojunction between the two types of materials. "Close" means that for an efficient device, the heterojunction should be reached within the exciton diffusion length. If this is not the case, the excitons recombine before they are separated into electrons and holes.

Since 2001, organic bulk heterojunction solar cells have seen a steep increase in efficiency (from about 2% to 11%), mainly driven by the optimization of energy levels, in order to maximize light absorption as well as to minimize energy and recombination losses at the heterojunction. Future work will most likely focus on achieving enhanced electrical properties to allow charge extraction from thicker devices and to improve device stability.

## 1.5 Conclusions

The last 5 years have seen an amazing development in thin-film photovoltaics in terms of efficiency increase, in terms of new material options, and in terms of an improved understanding of processes and devices. This is true for the classical inorganic thin-film devices where, after more than 30 years of research performed, major progress in efficiencies has been demonstrated. Organic solar cells strive toward improved manufacturability. And finally a new class of materials, organic–inorganic metal halides with an unprecedented development of efficiencies, have opened an entirely new window of opportunity.

As a consequence the size of the scientific community concerned with thin-film photovoltaics is still increasing. In addition, more and more specialists for sophisticated physical and chemical analysis methods enter the field, improving our common understanding. Since photovoltaic devices are complex multicomponent systems, the most satisfying answers always will arise from a combination of a solid understanding of the photovoltaic principles with the results from various methods analyzing the electronic, chemical, and structural properties of all the layers and interfaces in the device.

### Acknowledgments

The authors would like to thank Dorothea Lennartz for help with the figures. Special thanks are due to Bart Pieters (FZ Jülich) and Stephan Bücheler (EMPA) for discussions on thin-film silicon and CdTe solar cells.

## References


1. Shockley, W. and Queisser, H.J. (1961) Detailed balance limit of efficiency of p-n junction solar cells. *J. Appl. Phys.*, **32**, 510.
2. aWürfel, P. (1982) The chemical potential of radiation. *J. Phys. C*, **15**, 3967–3985.
3. Bridgman, P.W. (1928) Note on the principle of detailed balancing. *Phys. Rev.*, **31**, 101.
4. Rau, U. and Werner, J.H. (2004) Radiative efficiency limits of solar cells with lateral band-gap fluctuations. *Appl. Phys. Lett.*, **84**, 3735–3737.
5. Mattheis, J., Werner, J.H., and Rau, U. (2008) Finite mobility effects on the radiative efficiency limit of pn-junction solar cells. *Phys. Rev. B*, **77**, 085203.
6. Rau, U. (2007) Reciprocity relation between photovoltaic quantum efficiency and electroluminescent emission of solar cells. *Phys. Rev. B*, **76**, 085303.
7. Kirchartz, T. and Rau, U. (2008) Detailed balance and reciprocity in solar cells. *Phys. Status Solidi A*, **205**, 2737–2751.
8. Green, M.A. (2002) Lambertian light trapping in textured solar cells and light-emitting diodes: analytical solutions. *Prog. Photovolt. Res. Appl.*, **10**, 235.
9. Mattheis, J. (2008) Mobility and homogeneity effects on the power conversion efficiency of solar cells. Dissertation, Universität Stuttgart. http://elib.uni-stuttgart.de/opus/volltexte/2008/3697/ (accessed 23 February 2010).
10. Tiedje, T., Yablonovitch, E., Cody, G.D., and Brooks, B.G. (1984) Limiting efficiency of silicon solar cells. *IEEE Trans. Electron Devices*, **31**, 711.
11. Würfel, P. (2002) *Physica E*, **14**, 18–26.
12. Green, M.A. (1984) Limits on the open-circuit voltage and efficiency of silicon solar cells imposed by intrinsic Auger processes. *IEEE Trans. Electron Devices*, **31**, 671.
13. Hall, R.N. (1952) Electron–hole recombination in Germanium. *Phys. Rev.*, **87**, 387.
14. Shockley, W. and Read, W.T. (1952) Statistics of the recombinations of holes and electrons. *Phys. Rev.*, **87**, 835.
15. Auger, P. (1925) Sur L'effet photoélectrique composé. *J. Phys. Radium*, **6**, 205.
16. Meitner, L. (1922) Über die β-strahlspektra und ihren zusammenhang mit der γ-strahlung. *Z. Phys. A Hadrons Nucleic*, **11**, 35.
17. Dersch, H., Stuke, J., and Beichler, J. (1981) Light-induced dangling bonds in hydrogenated amorphous silicon. *Appl. Phys. Lett.*, **38**, 456.
18. Tiedje, T., Cebulka, J.M., Morel, D.L., and Abeles, B. (1981) Evidence for exponential band tails in amorphous silicon hydride. *Phys. Rev. Lett.*, **46**, 1425.
19. Schiff, E.A. (1981) Trap-controlled dispersive transport and exponential band tails in amorphous silicon. *Phys. Rev. B*, **24**, 6189.
20. Fedders, P.A., Drabold, D.A., and Nakhmanson, S. (1998) Theoretical study on the nature of band tail states in amorphous Si. *Phys. Rev. B*, **58**, 15624.
21. Poortmans, J. and Arkhipov, V. (eds) (2006) *Thin Film Solar Cells – Fabrication, Characterization and Applications*, John Wiley & Sons, Ltd, Chichester.
22. Hamakawa, Y. (ed) (2004) *Thin-Film Solar Cells: Next Generation Photovoltaics and Its Applications*, Springer, Berlin.
23. Chopra, K.L., Paulson, P.D., and Dutta, V. (2004) Thin-film solar cells: an overview. *Prog. Photovolt. Res. Appl.*, **12**, 69.
24. Siebentritt, S. and Rau, U. (eds) (2006) *Wide-Gap Chalcopyrites*, Springer, Berlin.
25. Rau, U. and Schock, H.W. (2015) Cu(in,Ga)$Se_2$ and related solar cells, in *Clean Electricity from Photovoltaics*, 2nd edn (eds M.D. Archer and M.A. Green), Imperial College Press, London, p. 245.

26. Jaegermann, W., Klein, A., and Mayer, T. (2009) Interface engineering of inorganic thin-film solar cells – materials-science challenges for advanced physical concepts. *Adv. Mater.*, **21**, 4196.
27. Street, R.A. (1991) *Hydrogenated Amorphous Silicon*, Cambridge University Press.
28. Ballif, C., Despeisse, M., and Haug, F.-J. (2015) Thin-film solar cells based on amorphous and microcrystalline silicon, in *Clean Electricity from Photovoltaics*, 2nd edn (eds M.D. Archer and M.A. Green), Imperial College Press, London, p. 139.
29. Zeman, M. and Schropp, R.E.I. (1998) *Amorphous and Microcrystalline Silicon Solar Cells: Modeling, Materials and Device Technology*, Kluwer Academic Publishers, Norwell.
30. Shah, A.V., Schade, H., Vanecek, M., Meier, J., Vallat-Sauvain, E., Wyrsch, N., Kroll, U., Droz, C., and Bailat, J. (2004) Thin-film silicon solar cell technology. *Prog. Photovolt. Res. Appl.*, **12**, 113.
31. Schropp, R.E.I., Carius, R., and Beaucarne, G. (2007) Amorphous silicon, microcrystalline silicon, and thin-film polycrystalline silicon solar cells. *MRS Bull.*, **32**, 219.
32. Deng, X. and Schiff, E.A. (2003) Measurement amorphous silicon-based solar cells, in *Handbook of Photovoltaic Science and Engineering* (eds A. Luque and S. Hegedus), John Wiley & Sons, Ltd, Chichester, p. 505.
33. Baranovski, S. (ed) (2006) *Charge Transport in Disordered Solids – With Applications in Electronics*, John Wiley & Sons, Ltd, Chichester.
34. Ito, K. (2014) *Copper Zinc Tin Sulfide-Based Thin-Film Solar Cells*, John Wiley & Sons, Ltd, Chichester.
35. Siebentritt, S. and Schorr, S. (2012) Kesterites – a challenging material for solar cells. *Prog. Photovolt. Res. Appl.*, **20**, 512.
36. Stranks, S.D. and Snaith, H.J. (2015) Metal-halide perovskites for photovoltaic and light-emitting devices. *Nat. Nanotechnol.*, **10**, 391.
37. Green, M.A., Ho-Baillie, A., and Snaith, H.J. (2014) The emergence of perovskite solar cells. *Nat. Photonics*, **8**, 506.
38. Credgington, D. (2015) Organic photovoltaics, in *Clean Electricity from Photovoltaics*, 2nd edn (eds M.D. Archer and M.A. Green), Imperial College Press, London, p. 339.
39. Reynolds, D.C., Leies, G., Antes, L.L., and Marburger, R.E. (1954) Photovoltaic effect in cadmium sulfide. *Phys. Rev.*, **96**, 533.
40. Böer, K.W. (1976) Photovoltaic effect in CdS-$Cu_2S$ heterojunctions. *Phys. Rev. B*, **13**, 5373.
41. Böer, K.W. and Rothwarf, A. (1976) Materials for solar photovoltaic energy conversion. *Annu. Rev. Mater. Sci.*, **6**, 303.
42. Pfisterer, F. (2003) The wet-topotaxial process of junction formation and surface treatments of $Cu_2S$–CdS thin-film solar cells. *Thin Solid Films*, **431–432**, 470.
43. Migliorato, P., Tell, B., Shay, J.L., and Kasper, H.M. (1974) Junction electroluminescence in $CuInSe_2$. *Appl. Phys. Lett.*, **24**, 227.
44. Wagner, S., Shay, J.L., Migliorato, P., and Kasper, H.M. (1974) $CuInSe_2$/CdS heterojunction photovoltaic detectors. *Appl. Phys. Lett.*, **25**, 434.
45. Shay, J.L., Wagner, S., and Kasper, H.M. (1975) Efficient $CuInSe_2$/CdS solar cells. *Appl. Phys. Lett.*, **27**, 89.
46. Jackson, P., Hariskos, D., Wuerz, R., Kiowski, O., Bauer, A., Friedlmeier, T.M., and Powalla, M. (2015) Properties of Cu(In,Ga)$Se_2$ solar cells with new record efficiencies up to 21.7%. *Phys. Status Solidi RRL*, **9**, 28.
47. Mickelsen, R.A. and Chen, W.S. (1980) High photocurrent polycrystalline thin-film CdS/$CuInSe_2$ solar cell. *Appl. Phys. Lett.*, **36**, 371–373.
48. Gabor, A.M., Tuttle, J.R., Albin, D.S., Contreras, M.A., Noufi, R., Jensen, D.G., and Hermann, A.M. (1994) High-efficiency $CuIn_xGa_{1-x}Se_2$ solar cells from $(In_xGa_{1-x})_2Se_3$ precursors. *Appl. Phys. Lett.*, **65**, 198–200.
49. Binsma, J.J.M. and Van der Linden, H.A. (1982) Preparation of thin $CuInS_2$

films via a two-stage process. *Thin Solid Films*, **97**, 237–243.

50. Probst, V., Karg, F., Rimmasch, J., Riedl, W., Stetter, W., Harms, H., and Eibl, O. (1996) Advanced stacked elemental layer progress for Cu(InGa)$Se_2$ thin film photovoltaic devices. *Mat. Res. Soc. Symp. Proc.*, **426**, 165–176.
51. Stolt, L., Hedström, J., Kessler, J., Ruckh, M., Velthaus, K.O., and Schock, H.W. (1993) ZnO/CdS/$CuInSe_2$ thin-film solar cells with improved performance. *Appl. Phys. Lett.*, **62**, 597–599.
52. Holz, J., Karg, F., and von Phillipsborn, H. (1994) *The Effect of Substrate Impurities on the Electronic Conductivity in CIGS Thin Films*. Proceedings of the 12th European Photovoltaic Solar Energy Conference, Amsterdam. H. S. Stephens & Associates, Bedford, pp. 1592–1595.
53. Nakada, T., Iga, D., Ohbo, H., and Kunioka, A. (1997) Effects of sodium on Cu(In,Ga)$Se_2$-based thin films and solar cells. *Jpn. J. Appl. Phys.*, **36**, 732–737.
54. Rocket, A. (2005) The effect of Na in polycrystalline and epitaxial single-crystal $CuIn_{1-x}Ga_xSe_2$. *Thin Solid Films*, **480**, 2–7.
55. Siebentritt, S., Igalson, M., Persson, C., and Lany, S. (2010) The electronic structure of chalcopyrite-bands, point defects and grain boundaries. *Prog. Photovolt. Res. Appl.*, **18**, 390.
56. Dirnstorfer, I., Wagner, M., Hofmann, D.M., Lampert, M.D., Karg, F., and Meyer, B.K. (1998) Characterization of CuIn(Ga)$Se_2$ thin films – II. In-rich layers. *Phys. Status Solidi A*, **168**, 163–175.
57. Bauknecht, A., Siebentritt, S., Albert, J., and Lux-Steiner, M.C. (2001) Radiative recombination via intrinsic defects in $Cu_xGa_ySe_2$. *J. Appl. Phys.*, **89**, 4391–4400.
58. Rau, U., Schmitt, M., Parisi, J., Riedl, W., and Karg, F. (1998) Persistent photoconductivity in Cu(In,Ga)$Se_2$ heterojunctions and thin films prepared by sequential deposition. *Appl. Phys. Lett.*, **73**, 223–225.
59. Lany, S. and Zunger, A. (2008) Intrinsic DX centers in ternary chalcopyrite semiconductors. *Phys. Rev. Lett.*, **100**, 016401.
60. Rau, U., Taretto, K., and Siebentritt, S. (2009) Grain boundaries in Cu(In,Ga)$(Se,S)_2$ thin-film solar cells. *Appl. Phys. A*, **96**, 221–234.
61. Schmid, D., Ruckh, M., Grunwald, F., and Schock, H.W. (1993) Chalcopyrite/defect chalcopyrite heterojunctions on basis of $CuInSe_2$. *J. Appl. Phys.*, **73**, 2902–2909.
62. Morkel, M., Weinhardt, L., Lohmüller, B., Heske, C., Umbach, E., Riedl, W., Zweigart, S., and Karg, F. (2001) Flat conduction-band alignment at the CdS/$CuInSe_2$ thin-film solar-cell heterojunction. *Appl. Phys. Lett.*, **79**, 4482–4484.
63. Dullweber, T., Hanna, G., Rau, U., and Schock, H.W. (2001) A new approach to high-efficiency solar cells by band gap grading in Cu(In,Ga)$Se_2$ chalcopyrite semiconductors. *Sol. Energy Mater. Sol. Cells*, **67**, 1–4.
64. Turcu, M., Pakma, O., and Rau, U. (2002) Interdependence of absorber composition and recombination mechanism in Cu(In,Ga)$(Se,S)_2$ heterojunction solar cells. *Appl. Phys. Lett.*, **80**, 2598–2600.
65. Kötschau, I.M. and Schock, H.W. (2003) Depth profile of the lattice constant of the Cu-poor surface layer in $(Cu_2Se)_{1-x}(In_2Se_3)_x$, evidenced by grazing incidence X-ray diffraction. *J. Phys. Chem. Solids*, **64**, 1559–1563.
66. Nguyen, Q., Orgassa, K., Koetschau, I., Rau, U., and Schock, H.W. (2003) Influence of heterointerfaces on the performance of Cu(In,Ga)$Se_2$ solar cells with CdS and In$(OH_x,S_y)$ buffer layers. *Thin Solid Films*, **431**, 330–334.
67. Weinhardt, L., Heske, C., Umbach, E., Niesen, T.P., Visbeck, S., and Karg, F. (2004) Band alignment at the i-ZnO/CdS interface in Cu(In,Ga)$(S,Se)_2$ thin-film solar cells. *Appl. Phys. Lett.*, **84**, 3175–3177.
68. Hariskos, D., Spiering, S., and Powalla, M. (2005) Buffer layers in Cu(In,Ga)Se-2 solar cells and modules. *Thin Solid Films*, **480**, 99–109.

69. Nakada, T. and Mizutani, M. (2002) 18% efficiency Cd-free Cu(In, Ga)$Se_2$ thin-film solar cells fabricated using chemical bath deposition (CBD)-ZnS buffer layers. *Jpn. J. Appl. Phys.*, **41**, L165–L167.
70. Hariskos, D., Fuchs, B., Menner, R., Naghavi, N., Hubert, C., Lincot, D., and Powalla, M. (2009) The Zn(S,O,OH)/ZnMgO buffer in thin-film Cu(In,Ga)$(Se,S)_2$-based solar cells part II: magnetron sputtering of the ZnMgO buffer layer for in-line co-evaporated Cu(In,Ga)$Se_2$ solar cells. *Prog. Photovolt. Res. Appl.*, **17**, 479–488.
71. Cusano, D.A. (1963) CdTe solar cells and photovoltaic heterojunctions in II–VI compounds. *Solid State Electron.*, **6**, 217.
72. Bonnet, D. (2004) *The Evolution of the CdTe Thin Film Solar Cell*. Proceedings of the European Photovoltaic Solar Energy Conference, June 2004, Paris. WIP Renewable Energies, Munich, p. 1657.
73. Bonnet, D. and Rabenhorst, H. (1972) *New Results on the Development of a Thin Film p-CdTe/n-CdS Heterojunction Solar Cell*. Proceedings of the 9th IEEE Photovoltaic Specialists Conference, May 1972, Silver Springs, MD. IEEE, New York.
74. First Solar, Inc. (2015) First solar achieves efficiency, durability milestones. Press release, February 15. http://investor.firstsolar.com/releasedetail.cfm?ReleaseID=895118 (accessed 23 February 2016).
75. http://www.ise.fraunhofer.de/de/downloads/pdf-files/aktuelles/photovoltaics-report-in-englischer-sprache.pdf.
76. McCandless, B.E., Qu, Y., and Birkmire, R.W. (1994) *A Treatment to Allow Contacting CdTe with Different Conductors*. Proceedings of the 24th IEEE Photovoltaic Specialists Conference. December 1994, Waikoloa, Hawaii, IEEE pp. 107–110.
77. Moutinho, H.R., Al-Jassim, M.M., Levi, D.H., Dippo, P.C., and Kazmerski, L.L. (1998) Effects of $CdCl_2$ treatment on the recrystallization and electro-optical properties of CdTe thin films. *J. Vac. Sci. Technol.*, **16**, 1251–1257.
78. Dobson, K.D., Visoly-Fischer, I., Hodes, G., and Cahen, D. (2000) Stability of CdTe/CdS thin-film solar cells. *Sol. Energy Mater. Sol. Cells*, **62**, 295–325.
79. Romeo, N., Bosio, A., Canevari, V., and Podesta, A. (2005) Recent progress on CdTe/CdS thin film solar cells. *Sol. Energy*, **77**, 795–801.
80. Bätzner, D.L., Romeo, A., Zogg, H., Tiwari, A.N., and Wendt, R. (2000) *Thin Solid Films*, **361–362**, 463–467.
81. Kranz, L., Gretener, C., Perrenoud, J., Schmitt, R., Pianezzi, F., La Mattina, F., Blösch, P., Cheah, E., Chirila, A., Fella, C.M., Hagendorfer, H., Jäger, T., Nishiwaki, S., Uhl, A.R., Buecheler, S., and Tiwari, A.N. (2013) Doping of polycrystalline CdTe for high-efficiency solar cells on flexible metal foil. *Nat. Commun.*, **4**, 2306–2312.
82. Fritsche, J., Kraft, D., Thissen, A., Mayer, T., Klein, A., and Jaegermann, W. (2002) Band energy diagram of CdTe thin film solar cells. *Thin Solid Films*, **403–404**, 252–257.
83. Visoly-Fisher, I., Cohen, S.R., Gartsman, K., Ruzin, A., and Cahen, D. (2006) Understanding the beneficial role of grain boundaries in polycrystalline solar cells from single-grain-boundary scanning probe microscopy. *Adv. Funct. Mater.*, **16**, 649–660.
84. Schorr, S. (2014) Crystallographic aspects of $Cu_2ZnSnS_4$ (CZTS), in *Copper Zinc Tin Sulfide-Based Thin-Film Solar Cells* (ed K. Ito), John Wiley & Sons, Ltd, Chichester.
85. Adachi, S. (2014) Physical properties, in *Copper Zinc Tin Sulfide-Based Thin-Film Solar Cells* (ed K. Ito), John Wiley & Sons, Ltd, Chichester.
86. Shin, B., Gunawan, O., Zhu, Y., Bojarczuk, N.A., Chey, S.J., and Guha, S. (2011) Thin film solar cell with 8.4% power conversion efficiency using an earth-abundant $Cu_2ZnSnS_4$ absorber. *Prog. Photovolt. Res. Appl.*, **21**, 72.
87. Repins, I., Beall, C., Vora, N., DeHart, C., Kuciauskas, D., Dippo, P., To, B., Mann, J., Hsu, W.C., Goodrich, A., and Noufi, R. (2012) Co-evaporated

$Cu_2ZnSnSe_4$ films and devices. *Sol. Energy Mater. Sol. Cells*, **101**, 154.

88. Wang, W., Winkler, M.T., Gunawan, O., Gokmen, T., Todorov, T.K., Zhu, Y., and Mitzi, D.B. (2014) Device characteristics of CZTSSe thin film solar cell with 12.6% efficiency. *Adv. Energy Mater.*, **4**, 1301465.
89. Dudchak, I.V. and Piskach, L.V. (2003) Phase equilibria in the $Cu_2SnSe_3-SnSe_2-ZnSe$ system. *J. Alloys Compd.*, **351**, 145.
90. Olekseyuk, I.D., Dudchak, I.V., and Piskach, L.V. (2004) Phase equilibria in the $Cu_2S-ZnS-SnS_2$ system. *J. Alloys Compd.*, **368**, 135.
91. Siebentritt, S. (2013) Why are kesterite solar cells not 20% efficient? *Thin Solid Films*, **535**, 1.
92. Pieters, B.E., Stiebig, H., Zeman, M., and van Swaaij, R.A.C.M. (2009) Determination of the mobility gap of μc-Si:H in pin solar cells. *J. Appl. Phys.*, **105**, 044502.
93. Street, R.A. (1991) *Hydrogenated Amorphous Silicon*, Cambridge University Press, pp. 363–403.
94. Chapin, D.M., Fuller, C.S., and Pearson, G.L. (1954) A new silicon p–n junction photocell for converting solar radiation into electrical power. *J. Appl. Phys.*, **25**, 676.
95. Carlson, D.E. and Wronski, C.R. (1976) Amorphous silicon solar cell. *Appl. Phys. Lett.*, **28**, 671.
96. Chittick, R.C., Alexander, J.H., and Sterling, H.F. (1969) The preparation and properties of amorphous silicon. *J. Electrochem. Soc.*, **116**, 77.
97. Spear, W.E. and LeComber, P.G. (1975) Substitutional doping of amorphous silicon. *Solid State Commun.*, **17**, 1193.
98. Zeman, M. (2006) Advanced amorphous silicon solar cell technology, in *Thin Film Solar Cells – Fabrication, Characterization and Applications* (eds J. Poortmans and V. Arkhipov), John Wiley & Sons, Ltd, Chichester, p. 204.
99. Staebler, D.L. and Wronski, C.R. (1977) Reversible conductivity changes in discharge-produced amorphous Si. *Appl. Phys. Lett.*, **31**, 292.
100. de Walle, C.G.V. and Street, R.A. (1995) Silicon–hydrogen bonding and hydrogen diffusion in amorphous silicon. *Phys. Rev. B*, **51**, 10615.
101. Stutzmann, M., Jackson, W.B., and Tsai, C.C. (1986) Annealing of metastable defects in hydrogenated amorphous silicon. *Phys. Rev. B*, **34**, 63.
102. Powell, M.J., Deane, S.C., and Wehrspohn, R.B. (2002) Microscopic mechanisms for creation and removal of metastable dangling bonds in hydrogenated amorphous silicon. *Phys. Rev. B*, **66**, 155212.
103. Branz, H. (1999) Hydrogen collision model: quantitative description of metastability in amorphous silicon. *Phys. Rev. B*, **59**, 5498.
104. Veprek, S., Marecek, V., and Anna Selvan, J.A. (1968) The preparation of thin layers of Ge and Si by chemical hydrogen plasma transport. *Solid State Electron.*, **11**, 683.
105. Usui, S. and Kikuchi, M. (1979) Properties of heavily doped GD-Si with low resistivity. *J. Non-Cryst. Sol.*, **34**, 1.
106. Kroll, U., Meier, J., Keppner, H., Littlewood, S.D., Kelly, I.E., Giannoulès, P., and Shah, A. (1995) Origin and incorporation mechanism for oxygen contaminants in a-Si:H and mc-Si:H films prepared by the very high frequency (70 MHz) glow discharge technique. *Mater. Res. Soc. Symp. Proc.*, **377**, 39.
107. Kroll, U., Meier, J., Keppner, H., Littlewood, S.D., Kelly, I.E., Giannoulès, P., and Shah, A. (1995) Origins of atmospheric contamination in amorphous silicon prepared by very high frequency (70 MHz) glow discharge. *J. Vac. Sci. Technol, A*, **13**, 2742.
108. Torres, P., Meier, J., Flückiger, R., Kroll, U., Selvan, J.A.A., Keppner, H., Shah, A., Littlewood, S.D., Kelly, I.E., and Giannoulès, P. (1996) Device grade microcrystalline silicon owing to reduced oxygen contamination. *Appl. Phys. Lett.*, **69**, 1373.
109. Meier, J., Dubail, S., Flückiger, R., Fischer, D., Keppner, H., and Shah, A. (1994) *Intrinsic Microcrystalline Silicon – A Promising New Thin Film Solar Cell Material*. Proceedings of the

1st World Conference on Photovoltaic Energy Conversion, December 1994, Hawaii, IEEE Hawaii. p. 409.

**110.** Flückiger, R. (1995) Microcrystalline silicon thin-films deposited by VHF plasma for solar cell applications. PhD thesis. Institute of Microtechnology, University of Neuchatel.

**111.** Green, M.A. (2001) Third generation photovoltaics: ultra-high conversion efficiency at low cost. *Prog. Photovolt. Res. Appl.*, **9**, 123.

**112.** Henry, C.H. (1980) Limiting efficiencies of ideal single and multiple energy gap terrestrial solar cells. *J. Appl. Phys.*, **51**, 4494.

**113.** de Vos, A. (1980) Detailed balance limit of the efficiency of tandem solar cells. *J. Phys. D: Appl. Phys.*, **13**, 839.

**114.** Coutts, T.J., Ward, J.S., Young, D.L., Emery, K.A., Gessert, T.A., and Noufi, R. (2003) Critical issues in the design of polycrystalline, thin-film tandem solar cells. *Prog. Photovolt. Res. Appl.*, **11**, 359.

**115.** Varlamov, S., Dore, J., Evans, R., Ong, D., Eggleston, B., Kunz, O., Schubert, U., Young, T., Huang, J., Soderstrom, T., Omaki, K., Kim, K., Teal, A., Jung, M., Yun, J., Pakhuruddin, Z.M., Egan, R., and Green, M.A. (2013) Polycrystalline silicon on glass thin-film solar cells: a transition from solid-phase to liquid-phase crystallised silicon. *Sol. Energy Mater. Sol. Cells*, **119**, 246–255.

**116.** Becker, C., Amkreutz, D., Sontheimer, T., Preidel, V., Lockau, D., Haschke, J., Jogschies, L., Klimm, C., Merkel, J.J., Plocica, P., Steffens, S., and Rech, B. (2013) Polycrystalline silicon thin-film solar cells: status and perspectives. *Sol. Energy Mater. Sol. Cells*, **119**, 112–123.

**117.** Haschke, J., Amkreutz, D., Korte, L., Ruske, F., and Rech, B. (2014) Towards wafer quality crystalline silicon thin-film solar cells on glass. *Sol. Energy Mater. Sol. Cells*, **128**, 190–197.

**118.** Kojima, A., Teshima, K., Shirai, Y., and Miyasaka, T. (2009) Organometal halide perovskites as visible-light sensitizers for photovoltaic cells. *J. Am. Chem. Soc.*, **131**, 6050.

**119.** Ball, J.M., Lee, M.M., Hey, A., and Snaith, H.J. (2013) Low-temperature processed meso-superstructured to thin-film perovskite solar cells. *Energy Environ. Sci.*, **6**, 1739.

**120.** De Wolf, S., Holovsky, J., Moon, S.-J., Löper, P., Niesen, B., Ledinsky, M., Haug, F.-J., Yum, J.-H., and Ballif, C. (2014) Organometallic halide perovskites: sharp optical absorption edge and its relation to photovoltaic performance. *J. Phys. Chem. Lett.*, **5**, 1035.

**121.** Yang, W.S., Noh, J.H., Jeon, N.J., Kim, Y.C., Ryu, S., Seo, J., and Seok, S.I. (2015) High-performance photovoltaic perovskite layers fabricated through intramolecular exchange. *Science*, **348**, 1234.

**122.** Ahn, N., Son, D.-Y., Jang, I.-H., Kang, S.M., Choi, M., and Park, N.-G. (2015) Highly reproducible perovskite solar cells with average efficiency of 18.3% and best efficiency of 19.7% fabricated via Lewis base adduct of lead(II) iodide. *J. Am. Chem. Soc.*, **137**, 8696.

**123.** Wehrenpfennig, C., Eperon, G.E., and Johnston, M.B. (2014) High charge carrier mobilities and lifetimes in organolead trihalide perovskites. *Adv. Mater.*, **26**, 1584.

**124.** Yin, W.-J., Shi, T., and Yan, Y. (2014) Unusual defect physics in $CH_3NH_3PbI_3$ perovskite solar cell absorber. *Appl. Phys. Lett.*, **104**, 063903.

**125.** Tvingstedt, K., Malinkiewicz, O., Baumann, A., Deibel, C., Snaith, H.J., Dyakonov, V., and Bolink, H.J. (2014) Radiative efficiency of lead iodide based perovskite solar cells. *Sci. Rep.*, **4**, 6071.

**126.** Xiao, Z., Yuan, Y., Shao, Y., Wang, Q., Dong, Q., Bi, C., Sharma, P., Gruverman, A., and Huang, J. (2015) Giant switchable photovoltaic effect in organometal trihalide perovskite devices. *Nat. Mater.*, **14**, 193.

**127.** Snaith, H.J., Abate, A., Ball, J.M., Eperon, G.E., Leijtens, T., Noel, N.K., Stranks, S.D., Wang, J.T.-W., Wojciechowski, K., and Zhang, W. (2014) Anomalous hysteresis in perovskite solar cells. *J. Phys. Chem. Lett.*, **5**, 1511.

**128.** Boix, P.P., Agarwala, S., Koh, T.M., Mathews, N., and Mhaisalkar, S.G. (2015) Perovskite solar cells: beyond

methylammonium lead iodide. *J. Phys. Chem. Lett.*, **6**, 898.

**129.** O'Reagen, B. and Gratzel, M. (1999) A low-cost, high-efficiency solar cell based on dye-sensitized colloidal $TiO_2$ films. *Nature*, **353**, 737.

**130.** Yu, G., Gao, J., Hummelen, J.C., Wudl, F., and Heeger, A.J. (1995) Polymer photovoltaic cells: enhanced efficiencies via a network of internal donor–acceptor heterojunctions. *Science*, **270**, 1789.

**131.** Peumans, P., Uchida, S., and Forrest, S.R. (2003) Efficient bulk heterojunction photovoltaic cells using small-molecular-weight organic thin films. *Nature*, **425**, 158.

**132.** Huynh, W.U., Dittmer, J.J., and Alivisatos, A.P. (2002) Hybrid nanorod-polymer solar cells. *Science*, **295**, 2425.

**133.** Sun, Y., Welch, G.C., Leong, W.L., Takacs, C.J., Bazan, G.C., and Heeger, A.J. (2012) Solution-processed small-molecule solar cells with 6.7% efficiency. *Nat. Mater.*, **11**, 44.

**134.** Cnops, K., Rand, B.P., Cheyns, D., Verreet, B., Empl, M.A., and Heremans, P. (2014) 8.4% efficient fullerene-free organic solar cells exploiting long-range exciton energy transfer. *Nat. Commun.*, **5**, 3406.